Journal of the Mechanics and Physics of Solids 64 (2014) 223–235

Contents lists available at ScienceDirect

Journal of the Mechanics and Physics of Solids

journal homepage: www.elsevier.com/locate/jmps

Impact comminution of solids due to local kinetic energy of high shear strain rate: I. Continuum theory and turbulence analogy

Zdeněk P. Bažant [a,*], Ferhun C. Caner [b]

[a] Northwestern University, 2145 Sheridan Road, CEE/A135, Evanston, IL 60208, United States
[b] Institute of Energy Technologies, Technical University of Catalonia, Av. Diagonal 647, 08028 Barcelona, Spain

ARTICLE INFO

Article history:
Received 21 July 2013
Received in revised form
11 November 2013
Accepted 13 November 2013
Available online 25 November 2013

Keywords:
Fracture mechanics
Dynamic fracture
Fragmentation
Effective viscosity
Penetration

ABSTRACT

The modeling of high velocity impact into brittle or quasibrittle solids is hampered by the unavailability of a constitutive model capturing the effects of material comminution into very fine particles. The present objective is to develop such a model, usable in finite element programs. The comminution at very high strain rates can dissipate a large portion of the kinetic energy of an impacting missile. The spatial derivative of the energy dissipated by comminution gives a force resisting the penetration, which is superposed on the nodal forces obtained from the static constitutive model in a finite element program. The present theory is inspired partly by Grady's model for expansive comminution due to explosion inside a hollow sphere, and partly by analogy with turbulence. In high velocity turbulent flow, the energy dissipation rate gets enhanced by the formation of micro-vortices (eddies) which dissipate energy by viscous shear stress. Similarly, here it is assumed that the energy dissipation at fast deformation of a confined solid gets enhanced by the release of kinetic energy of the motion associated with a high-rate shear strain of forming particles. For simplicity, the shape of these particles in the plane of maximum shear rate is considered to be regular hexagons. The particle sizes are assumed to be distributed according to the Schuhmann power law. The condition that the rate of release of the local kinetic energy must be equal to the interface fracture energy yields a relation between the particle size, the shear strain rate, the fracture energy and the mass density. As one experimental justification, the present theory agrees with Grady's empirical observation that, in impact events, the average particle size is proportional to the $(-2/3)$ power of the shear strain rate. The main characteristic of the comminution process is a dimensionless number B_a (Eq. (37)) representing the ratio of the local kinetic energy of shear strain rate to the maximum possible strain energy that can be stored in the same volume of material. It is shown that the kinetic energy release is proportional to the (2/3)-power of the shear strain rate, and that the dynamic comminution creates an apparent material viscosity inversely proportional to the (1/3)-power of that rate. After comminution, the interface fracture energy takes the role of interface friction, and it is pointed out that if the friction depends on the slip rate the aforementioned exponents would change. The effect of dynamic comminution can simply be taken into account by introducing the apparent viscosity into the material constitutive model, which is what is implemented in the paper that follows.

* Corresponding author. Tel.: +1 847 491 4025; fax: +1 847 491 4011.
E-mail addresses: z-bazant@northwestern.edu (Z.P. Bažant), ferhun.caner@upc.edu (F.C. Caner).

0022-5096/$ - see front matter © 2013 Elsevier Ltd. All rights reserved.
http://dx.doi.org/10.1016/j.jmps.2013.11.008

1. Introduction

In spite of the recent advances in the constitutive modeling of concrete, the finite element models for impact of missiles onto the walls of concrete structures often severely overestimate the depth of penetration and, in the case of perforation, the exit velocity. By contrast with impact on thin walls (<10 cm) or high rate tensile fracture, the penetration of thick walls causes comminution of a significant portion of concrete into fine particles ($0.01\ \mathrm{mm}^{-1}\,\mathrm{mm}$). The underestimation of the exit velocities and penetration depths is severe even when the finite element code uses a highly realistic constitutive model such as the new microplane model M7 (Caner and Bažant, 2013; Caner et al., 2013), which is an improvement of model M4 (Bažant et al., 2000) and provides very good fits of virtually the complete range of the experimental data from diverse types of uniaxial, biaxial and triaxial tests, including the tests of vertex effect, tensile and shear fracturing and the compression-shear behavior under very high confinement. The additional resistance to penetration due to the viscoelastic rate effect and to the rate-dependence of crack growth does not suffice by far for obtaining correct predictions of impact.

The macroscopic constitutive equation with softening damage, calibrated by standard laboratory tests at low strain rates, cannot describe material comminution into sub-mesoscale particles. It can capture only the energy dissipation by mesoscale fragmentation, i.e., the creation of fragments of the same order of magnitude as the dominant mesoscale material inhomogeneities, such as the largest aggregate pieces in concrete. This is the only kind of comminution that occurs in the standard laboratory tests of damage behavior. This limitation applies even if the constitutive equation is enhanced by the material rate effects, which include viscoelasticity and the rate dependence of mesoscale crack growth.

The purpose of the present paper is to show how a constitutive model can take into account the energy dissipated by material comminution at very high strain rates (see Fig. 1 adapted from Reinhardt and Weerheijm, 1991; Kipp et al., 1980). The spatial derivative of the energy dissipated by comminution represents a compressive force resisting the penetration, which has the effect of greatly increasing the finite element nodal forces obtained with a standard macroscopic constitutive model.

The literature on the analysis of impact is vast and great progress has been achieved in many directions (Mott, 1947; Grady and Kipp, 1979; Grady, 1982; Mescall and Weiss, 1984; Grady, 1985, 1990; Grady and Kipp, 1995; Camacho and Ortiz, 1996; Grady, 1998; Shih et al., 1998; Cadoni et al., 2001; Gailly and Espinosa, 2002; Gatuingt and Pijaudier-Cabot, 2002; Doyoyo, 2002; Forquin et al., 2008; Deshpande and Evans, 2008; Wei et al., 2009; Grady, 2010; Ferri et al., 2010; Kožar and Ožbolt, 2010; Adley et al., 2012; Ožbolt et al., 2011; Frank et al., 2012). As it appears, however, there exists no constitutive law that would capture the effect of material comminution and could be used to formulate an initial-boundary value problem underlying a finite element formulation. One important advance has been the development of the so-called "Mescall" models (Mescall and Weiss, 1984; Doyoyo, 2002; Deshpande and Evans, 2008; Wei et al., 2009; Kožar and Ožbolt, 2010; Ferri et al., 2010). But although they describe the nucleation and branching of dynamically propagating individual cracks they do not provide a constitutive model for a finite element code, describing the behavior of a material comminuting into a vast number of tiny fragments. The present work aims to provide for the Mescall zone an alternative model that is usable in finite element programs.

In the community of computational missile impact simulation, the recent work of Adley et al. (2012) and Frank et al. (2012) is worth noting. They adapted to high rate deformation a dynamic finite element code with microplane model M4 in which the strain-dependent strength limits (called stress–strain boundaries) were scaled up sharply so as to fit the test data on missile penetration. However, after this kind of purely empirical adjustment, the constitutive model used no longer fits the multitude of the standard uni-, bi-, and tri-axial laboratory tests of concrete by which the microplane model was calibrated. It also no longer fits (Ožbolt et al., 2011) high-rate tests of fracture specimens loaded dynamically in opening mode I, in which the high-rate deformation occurs almost exclusively in tension. These tests are in perfect agreement with the unadjusted microplane model M4 incorporating solely the quasi-static strain rate effects, which provide only a mild and smooth strength increase as the strain rate increases. The point to note is that, in contrast to missile impact, the notched specimens of Ožbolt and Reinhardt exhibit no material comminution. Adley et al.'s empirical adjustment thus loses

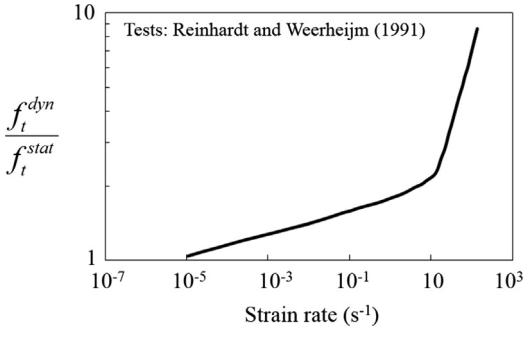

Fig. 1. Typical diagram of concrete tensile strength as a function of strain rate, roughly following the test data of Reinhardt and Weerheijm (1991).

predictive capability except for situations very similar to those for which the microplane strength limits have been adjusted.

The theory proposed here is partly inspired by analogy with turbulence. In high velocity turbulent flow, the energy dissipation rate is greatly enhanced by the formation of micro-vortices (eddies) which dissipate energy by viscous shear stress. By analogy, it is assumed that the energy dissipation at fast deformation of a confined solid gets greatly enhanced by the release of kinetic energy of high shear strain rate of forming particles. Another inspiration for the present model is Grady's model for explosion in a hollow sphere (Grady, 1982), in which the kinetic energy of volumetric strain is considered as the driving force of comminution. Grady calculated and experimentally justified that, in rapid volumetric expansion, the average particle size is

$$\bar{s} = \left(\frac{48\Gamma}{\rho \dot{\varepsilon}_V^2}\right)^{1/3} \tag{1}$$

where Γ is the interface fracture energy, ρ is the mass density and $\dot{\varepsilon}_V$ is the expansive volumetric strain rate. In later works (Grady, 1990; Grady and Kipp, 1995; Grady, 1998, 2010) he demonstrated by experiments that this equation can be extended to comminution under impact, but did not justify it theoretically. Here the extension of Grady's equation to impact is theoretically justified by noting that comminution under impact must be driven by the release of the local kinetic energy of shear strain rate. This basic idea is then used to develop a coherent constitutive model.

The presently proposed formulation is a continuum model that smears the sub-scale cracking. A number of continuum models that homogenize the sub-scale cracking of concrete, sea ice and other brittle heterogeneous materials have been proposed in the past (e.g. Bažant and Lin, 1988; Jirásek and Bažant, 1995). Gao and Klein (1998) and Klein and Gao (1998) consider a random network of cohesive bonds on the microscale and obtain the continuum model via the Cauchy–Born rule, i.e., by equating the strain energy of the continuum to the potential energy of the micro-scale bonds. However, all these models consider the fracturing to be caused by the release of strain energy. The present model is based on the fact that, at high rate deformation, it is the release of local kinetic energy that matters. This idea was outlined in a brief paper (Bažant and Caner, 2013) motivated by the recently proposed concept of shock fracturing of gas shale, and is here developed in detail.

This paper presents the theory. The following paper (Caner and Bažant, this issue) presents the numerical validation by large-scale finite element simulations of missile impact and by the simulation of Hopkinson bar tests of strength. These simulations use the microplane model M7 with comminution enhancement.

2. Local kinetic energy density of comminuting micro-particles at high shear rate

Consider first a simple idealized comminution process in which the material is comminuted to identical particles (Fig. 2a–d). The particles must fill the space completely. At first, we consider the particles to be identical. The only possible repetitive regular subdivisions of the material in the plane of maximum shearing are the squares, isosceles triangles, and regular hexagons. Among them, the hexagonal prisms are the likeliest as they have the least interface area per unit volume. More complex space-filling geometries, such as truncated octahedron, could be considered. But it turns out that the particle shape is not terribly important. It has no effect on the form of the resulting equations and causes only relatively small changes in their coefficients.

For graphical two-dimensional visualization, it is more instructive to begin discussion with a subdivision into squares (or cubes), as depicted in Fig. 2a for the undeformed state. During deformation, orthogonal coordinate axes x and y, along with the lines of the square subdivision (yet to occur), rotate by angle ω. Simultaneously, these lines get skewed relative to axes x and y by angles ε_D representing pure shear (Fig. 2b).

At a certain moment, the strain rate becomes high enough for the kinetic energy of deforming material to suffice for creating the fractures that rapidly comminute the material into separate identical square particles shown in Fig. 2c. As that happens, the particles regain their original undeformed shape, i.e., become squares again, while the centers of the comminuted particles still conform to the same macroscopic displacement field, which means that the dashed lines

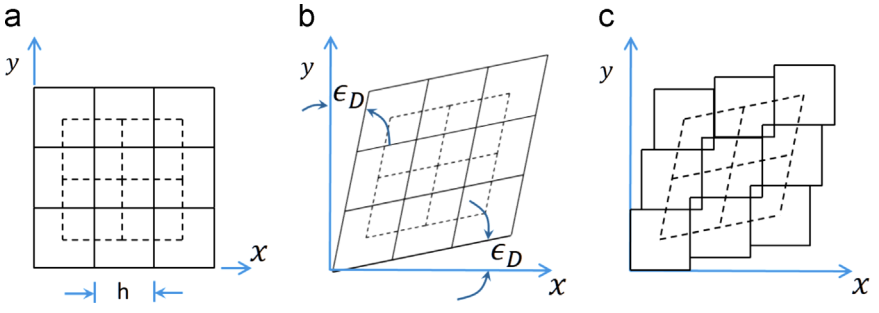

Fig. 2. Comminution of material into prismatic square particles, showing the velocities in terms of displacements during time Δt (note that displacements are supposed to be infinitesimal, in which case the overlaps at the square corners are second-order small and thus negligible).

connecting these centers are identical in Fig. 2b and c (we ignore the necessary crushing of the particle corners since their volume is second-order small).

As the particles return to their near-original shape, they release their kinetic energy $\Delta\mathcal{K}$ while the opposite faces of neighboring particles slip against each other, as marked by double arrows in Fig. 2c.

The global kinetic energy, which excludes the kinetic energy of shear strain rate of the particles, is in two dimensions, defined as

$$\overline{K} = \sum_i h^3 \frac{\rho}{2}(\dot{u}_0^2 + \dot{v}_0^2)_i \tag{2}$$

(where $\dot{u}_0, \dot{v}_0$ are the velocity components of the centers $i = 1, 2, 3, \ldots$ of the particles or of the eddies, and h is the side of the squares) remains unchanged as the particles separate.

For the subdivision of a plane into regular hexagons (Fig. 3a), we consider the particles in three dimensions to be hexagonal prisms of a length equal to the corner-to-corner diameter h of the hexagon. The volume of one particle and the interface area S of all the particles per unit volume of material are, respectively,

$$V_p = c_v h^3, \quad c_v = \frac{3\sqrt{3}}{8} \doteq 0.6495 \tag{3}$$

$$S = \frac{c_s}{h}, \quad c_s = 1 + \frac{4}{\sqrt{3}} \doteq 3.3094 \tag{4}$$

where c_s is the dimensionless constant. Note that since each two neighboring particles share the same interface, $S = \frac{1}{2} S_p / V_p$, where S_p is the surface area of one hexagonal prism.

Let the Cartesian coordinates x, y, z be placed so that plane (x,y) be the plane of maximum shear strain rate among all possible orientations. The field of displacements is considered to consist of pure shear strain ε_D and rotation ω. The maximum shear strain rate, denoted as $\dot{\varepsilon}_D$, is chosen to represent pure shear, in which case $\dot{\varepsilon}_D$ also represents the effective deviatoric strain rate, i.e.

$$\dot{\varepsilon}_D = \sqrt{\dot{\varepsilon}_{Dij}\dot{\varepsilon}_{Dij}/2} \tag{5}$$

(repetition of tensorial subscripts implies summation). Here ε_{Dij} is the deviatoric strain tensor in Cartesian coordinates, the superior dots denote the time derivatives, and the shear angle rate is $\dot{\gamma} = 2\dot{\varepsilon}_D$.

At first the hexagonal cells, not yet separated and of a size not yet known (Fig. 3b), undergo shear strain ε_D in conformity with the material as a whole. However, a quasibrittle material such as concrete cannot undergo a large strain and so, at a certain moment, the material will fracture into the hexagonal prisms. This sudden fracturing releases the strain in the hexagonal particles and allows them to regain their original shape. As they do, they must rotate against each other by angle ε_D (Fig. 3c).

It is considered that, during this whole process, the particle centers move so as to follow the field of macroscopic pure shear strain ε_D and simultaneous material rotation rate $\dot{\omega}$ (Fig. 3c) in plane (x,y). The effect of hydrostatic pressure will be included later. Explosive volume expansion, which leads to a different type of comminution, is not considered.

Before comminution, the displacement velocities $\dot{u}$ and $\dot{v}$ in the directions of current (Eulerian) coordinates x and y whose origin is placed into the particle center are, in the plane of maximum shear rate,

$$\dot{u} = \dot{u}_0 - \dot{\omega} y + \dot{\varepsilon}_D y, \quad \dot{v} = \dot{v}_0 + \dot{\omega} x + \dot{\varepsilon}_D x \tag{6}$$

After fracturing and separation of the particles these velocities change to

$$\dot{u}^+ = \dot{u}_0 - \dot{\omega} y, \quad \dot{v}^+ = \dot{v}_0 + \dot{\omega} x \tag{7}$$

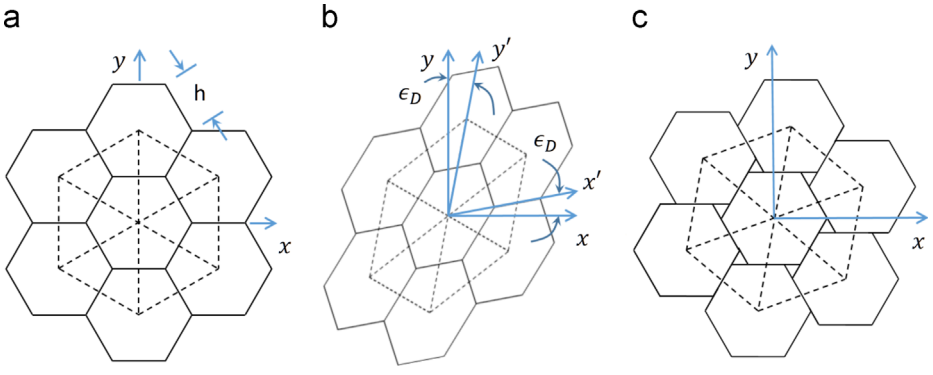

Fig. 3. Comminution of material into prismatic hexagonal particles, showing the velocities in terms of displacements during time Δt (note that displacements are supposed to be infinitesimal, in which case the gaps at the hexagon corners are second-order small and thus negligible).

The drop in kinetic energy of each cell is

$$-V_p\Delta\mathcal{K}=h\int_A\frac{\rho}{2}\left(\dot{u}^2+\dot{v}^2-(\dot{u}^+)^2-(\dot{v}^+)^2\right)\,\mathrm{d}A \tag{8}$$

$$-V_p\Delta\mathcal{K}=\frac{h\rho}{2}\dot{\varepsilon}_D^2\int_A(x^2+y^2)\,\mathrm{d}A+h\rho\int_A\left[\dot{v}_0\dot{\varepsilon}_D x+\dot{u}_0\dot{\varepsilon}_D y+\dot{\varepsilon}_D\dot{\omega}(x^2-y^2)\right]\mathrm{d}A \tag{9}$$

$$-V_p\Delta\mathcal{K}=\frac{h\rho}{2}\dot{\varepsilon}_D^2\int_A r^2\,\mathrm{d}A=\frac{h\rho}{2}I_p\,\dot{\varepsilon}_D^2 \tag{10}$$

or, per unit volume of material,

$$\Delta\mathcal{K}=-c_k\rho h^2\dot{\varepsilon}_D^2 \tag{11}$$

where

$$I_p=\frac{\sqrt{3}}{32}h^4\doteq 0.05413h^4,\quad c_k=\frac{I_p}{2hV_p}\doteq 0.04167 \tag{12}$$

here $\Delta\mathcal{K}$ is the drop of kinetic energy of the particle per unit volume, c_k is the dimensionless coefficient of kinetic energy, ρ is the mass density, A is the area of the hexagon, r is the radial coordinate, $I_p=I_x+I_y$ is the centroidal polar moment of inertia of the hexagon (and I_x, I_y is the moments of inertia about axes x and y, the orientation of which does not matter).

Note that, if the global motion is characterized by the velocities of particle centroids, the second integral in Eq. (9) vanishes. Actually this is exactly true only when $I_x=I_y$, which occurs for cubes, but only approximately for hexagons. Also note that the material rotation velocity $\dot{\omega}$ has no effect on $\mathcal{K}$. Indeed, it ought to be so, since rigid body rotations can cause no fracturing. Thus it is proven that the global and local kinetic energy densities are, in two dimensions, separable.

3. Separability of local and global kinetic energy in three dimensions

In three dimensions, the axial vector of local rotation rate, $\dot{\boldsymbol{\omega}}$, does not have to be orthogonal to plane (x,y) of maximum shear rate. It may be decomposed as

$$\dot{\boldsymbol{\omega}}=\dot{\boldsymbol{\omega}}_N+\dot{\boldsymbol{\omega}}_P \tag{13}$$

where $\dot{\boldsymbol{\omega}}_N,\dot{\boldsymbol{\omega}}_P$ are the axial vectors of the components normal to plane (x,y) of maximum shear and parallel to that plane. Instead of Eq. (8), the density difference between the total kinetic energy and the kinetic energy of corresponding to velocity vector $\boldsymbol{v}_0$ at particle center becomes

$$-V_p\Delta\mathcal{K}=\frac{\rho}{2}\int_{V_p}\left[(\boldsymbol{v}_0+\dot{\boldsymbol{\omega}}\times\boldsymbol{x}+\dot{\boldsymbol{\epsilon}}\cdot\boldsymbol{x})^2-(\boldsymbol{v}_0+\dot{\boldsymbol{\omega}}\times\boldsymbol{x})^2\right]\mathrm{d}V \tag{14}$$

$$-V_p\Delta\mathcal{K}=\frac{\rho}{2}\int_{V_p}(\dot{\boldsymbol{\epsilon}}\cdot\boldsymbol{x})^2\,\mathrm{d}V+\rho\int_{V_p}(\dot{\boldsymbol{\epsilon}}\cdot\boldsymbol{x})\cdot(\dot{\boldsymbol{\omega}}_N\times\boldsymbol{x})\,\mathrm{d}V+\rho\int_{V_p}(\dot{\boldsymbol{\epsilon}}\cdot\boldsymbol{x})\cdot(\dot{\boldsymbol{\omega}}_P\times\boldsymbol{x})\,\mathrm{d}V \tag{15}$$

where the integral of $\boldsymbol{v}_0\cdot(\dot{\boldsymbol{\epsilon}}\cdot\boldsymbol{x})$ has vanished by virtue of symmetry; $\dot{\boldsymbol{\epsilon}}$ is the strain rate tensor, $\dot{\boldsymbol{\epsilon}}\cdot\boldsymbol{x}$ is the strain rate vector on plane (x,y); and $\boldsymbol{x}$ is the vector of coordinates x,y centered at particle center. The second integral in Eq. (15) corresponds to rotation within plane (x,y) of maximum shear rate $\dot{\varepsilon}_D$, and so the first two integrals are equivalent to the previous two-dimensional analysis in Eq. (10).

The third integral in Eq. (15) corresponds to rotation in a plane normal to the plane (x,y) of maximum shear rate $\dot{\varepsilon}_D$. This integral is in general nonzero. But it seems impossible that a rotation in a plane normal to (x,y), i.e., a rotation about a vector lying in plane (x,y), could contribute to comminution in plane (x,y). It could affect comminution only in a plane normal to (x,y). Therefore, the kinetic energy corresponding to the last term in Eq. (15) can be ignored, and Eq. (11) should be applicable to all situations.

4. Partial analogy with turbulence

It is interesting that the kinetic energy $\mathcal{K}_{shear}$ of a particle deforming by pure shear at rate $\dot{\varepsilon}_D$ happens to be the same as the kinetic energy $\mathcal{K}_{eddy}$ of the same particle rotating as a rigid body at angular rate $\dot{\omega}=\dot{\varepsilon}_D$. Indeed, the squares of the velocity magnitudes in the comminuting particle with shear strain rate $\dot{\omega}_D$ and in a turbulence vortex (eddy) treated approximately as a small rigid domain of area A with angular flow velocity $\dot{\omega}$ can be used, respectively, to calculate the local kinetic energies:

$$\mathcal{K}_{shear}=\int_A\frac{\rho}{2}|\boldsymbol{v}|^2\,\mathrm{d}A=\int_A\frac{\rho}{2}\left[(\dot{\varepsilon}_D y)^2+(\dot{\varepsilon}_D x)^2\right]\mathrm{d}A \tag{16}$$

$$\mathcal{K}_{eddy}=\int_A\frac{\rho}{2}|\boldsymbol{v}|^2\,\mathrm{d}A=\int_A\frac{\rho}{2}\left[(\dot{\omega}y)^2+(\dot{\omega}x)^2\right]\mathrm{d}A \tag{17}$$

Now note that when $\dot{\omega} = \dot{\varepsilon}_D$,

$$\mathcal{K}_{shear} = \mathcal{K}_{eddy} \tag{18}$$

even though the velocity vectors at the corresponding points do not have the same directions.

This observation reveals a partial analogy with turbulence (Tennekes and Lumley, 1972), which is what inspired the present theory. In both comminution and turbulence, the micro-level kinetic energy (Eq. (16) or (17)) augments the kinetic energy of the macro-level part of the turbulent flow of a fluid, or the macrolevel kinetic energy of the assembly of the comminuting particles, which in both cases is equal to

$$\sum_i \frac{\rho}{2}(\dot{u}_0^2 + \dot{v}_0^2)_i \tag{19}$$

where $\dot{u}_0, \dot{v}_0$ denote the velocity components of the centers $i = 1, 2, 3, \ldots$ of the particles or of the eddies. The micro-level kinetic energy gets dissipated by fluid viscosity in the eddies of turbulent flow, or the by the energy of interface fracture of the comminuting particles. In both cases, minimization of the total energy of motion requires a micro-level energy dissipation mechanism consisting of eddy formation or comminution.

When the local motion of a shear strain field continues after the break of the interface, interface slips (like those from (b) to (c) in Fig. 3) must get repeated. But in contrast to the rotational motion in a turbulent eddy, the interface slips cannot continue indefinitely because the shear angle cannot be infinite.

5. Approximate generalization to randomly distributed particle sizes

Limiting consideration to micro-particles of one size would be an oversimplification. It is well-known that, in all sorts of dynamic comminution, the particle sizes vary randomly. The frequency distribution of particle sizes may approximately be described by Schuhmann's power law (Schuhmann, 1940; Charles, 1957; Ouchterlony, 2005; Cunningham, 1987). This law was found to give realistic results for, e.g., the particle sizes and the resisting force due to comminution of concrete slabs during the collapse of the World Trade Center towers (Bažant et al., 2008). The Schuhmann law is described by a power-law cumulative distribution function of particle size s:

$$F(s) = \frac{s^k - h^k}{H^k - h^k} \quad \left[s \in (h, H),\ F(s) \in (0, 1)\right] \tag{20}$$

where k is a empirical constant (typically $k \approx 0.5$), $h = s_{\min}$ is the minimum micro-particle size, and $H = s_{\max}$ is the maximum micro-particle size (usually $H/h = 10$–100). Other particle size distributions have also been used (Mott, 1947; Grady, 1990) and the analysis that follows can be readily adapted to any one of them.

Within the size interval $(s, s+\mathrm{d}s)$, the number of micro-particles per unit volume is $\mathrm{d}F(s)/s^3$. The average particle size is $\bar{s} = \int_h^H s\,\mathrm{d}F(s)$ or

$$\bar{s} = \bar{c}h \tag{21}$$

$$\text{where} \quad \bar{c} = \frac{k}{k+1}\frac{(H/h)^{k+1} - 1}{(H/h)^k - 1} \tag{22}$$

Since, for size s, the particle interface area per unit volume is c_s/s, the combined interface area of all the micro-particles or random sizes per unit volume is

$$S = \int_{s=h}^{H} \frac{c_s}{s}\,\mathrm{d}F(s) = \frac{C_s}{h} \tag{23}$$

$$\text{where} \quad C_s = \frac{c_s k}{k-1}\frac{(H/h)^{k-1} - 1}{(H/h)^k - 1} \tag{24}$$

C_s is a dimensionless constant. It may be checked (with the aid of L'Hospital rule) that the limit of Eq. (23) for $H/h \to 1$ is c_s, as it must.

Note that, in this calculation, we did not address the fact that particles of unequal sizes cannot all be hexagonal prisms. This means that their closest packing may leave some empty interparticle spaces and would thus require a certain volume dilation, and also that particles of diverse shapes will be created. For simplicity, we do not analyze this dilation and shape diversity.

To calculate the kinetic energy loss, we introduce the simplifying hypothesis that it is possible to superpose the contributions calculated for various uniform particle sizes as if the particles of each size were distributed regularly. The loss of kinetic energy of the particles of all the sizes per unit volume (dimension J/m^3 or N/m^2) may then be obtained, according to Eq. (11), as follows:

$$\Delta\mathcal{K} = -\int_{s=h}^{H} c_k \rho s^2 \dot{\varepsilon}_D^2\,\mathrm{d}F(s) \tag{25}$$

The integration yields

$$\Delta\mathcal{K} = -C_k \rho h^2 \dot{\varepsilon}_D^2 \tag{26}$$

$$\text{where} \quad C_k = \frac{k}{k+2}\frac{(H/h)^{k+2}-1}{(H/h)^k-1}c_k \tag{27}$$

C_s is a dimensionless constant. For the limit case of particles of one size h, one may check that $\lim_{H/h\to 1} C_k = c_k$, as required. To illustrate the effect of the choice of particle shape, assuming $H/h=100$, one obtains for hexagonal and cubical particles respectively $C_s=0.331$, 0.300 and $C_k=92.6$, 138.9. These differences are not large and the form of the equations remains the same.

6. Release of local kinetic energy of strain rate as the driving force of dynamic fracturing

The total energy of the comminuted particles per unit volume is

$$\mathcal{F} = \mathcal{K} + S\Gamma \tag{28}$$

where Γ is the interface fracture energy of the comminuting particles (dimension J/m^2 or N/m). To formulate the criterion of dynamic fracturing, one must choose between two theoretically possible forms:

$$\text{either} \quad \frac{\partial \mathcal{F}}{\partial S} = 0 \tag{29}$$

$$\text{or} \quad -\Delta K = S\Gamma \tag{30}$$

In the former case, by analogy to classical fracture mechanics, it is assumed that once the fracture is triggered in a part of surface S, it will propagate. In the latter case, it is assumed that the entire surface forms simultaneously. The latter case would apply if the continuum strain rate were so high that the duration of comminution would require the fracture to propagate faster than the maximum possible crack propagation rate, which is the Raleigh wave speed. The results of analysis for both cases are very similar and differ only in dimensionless empirical coefficients. In what follows we will consider that the former case applies. Thus, according to Eq. (29), it is required that

$$-\frac{\partial(\Delta\mathcal{K})}{\partial S} = -\frac{\partial(\Delta\mathcal{K})/\partial h}{\mathrm{d}S/\mathrm{d}h} = \Gamma \tag{31}$$

This equation is similar to that used in Grady's (1982) analysis of tensile comminution due to high volumetric strain rate in an explosion within the center of a hollow sphere (see also Freund, 1990, Eq. (8.7.3)). It is seen to be analogous to the energy release criterion of fracture mechanics. In fact, it could have been derived directly from the condition of criticality: When the comminution gets under way, the rate of release of kinetic energy (with respect to S) at the given kinematic constraint (i.e., at given $\dot{\varepsilon}_D$) must be equal to the surface energy Γ.

Note that Eq. (31) may also be considered as a special case of Eqs. (5.3.2) and (5.3.20) in Freund (1990) when the strain energy density is neglected. But these are valid only for moderately high strain rates in which the kinetic energy density does not exceed the strain energy density in the material by an order of magnitude or more.

Eq. (30) imposes an overall energy balance condition which does not ensure incremental energy balance and thus does not guarantee the interface fracture to begin. On the other hand, like in classical fracture mechanics, Eq. (31) means that as soon as energy balance is satisfied incrementally, the fracture can occur, and must occur if the kinetic energy density is increased further.

Substitution of Eqs. (26) and (23) into (31) and differentiation furnish the minimum particle size:

$$h = s_{\min} = \left(\frac{C_a \Gamma}{\rho \dot{\varepsilon}_D^2}\right)^{1/3} \tag{32}$$

$$\text{where} \quad C_a = \frac{c_s}{c_k}\frac{(k+2)}{(k-1)}\frac{(k-1)(H/h)^k - k(H/h)^{k-1}+1}{k(H/h)^{k+2}-(k+2)(H/h)^k+2} \tag{33}$$

If $H/h=100$, then $C_a=0.032$ for hexagonal prisms and $C_a=0.019$ for cubical prisms. Thus we see again that the precise particle shape does not make a large difference. According to Eq. (21), the average particle size is then obtained as $\bar{s} = \bar{c}h$.

The maximum particle size H is approximately known. It must be one order of magnitude smaller than d_a, i.e.,

$$H \approx 0.1 d_a \tag{34}$$

because fragmentation into particles of the same order of magnitude as d_a is covered by the constitutive law based on static material tests with post-peak softening. Therefore, H must be about 2–4 mm for normal concrete, and 0.05–2 mm for high strength concrete. Thus, to calculate h, one must substitute Eq. (32) into (33) and then solve the resulting nonlinear algebraic equation for h iteratively, e.g., by the Newton method. The ratio H/h then follows.

Eq. (32) agrees with Grady's formula (1), which was justified empirically by observations of particle sizes in impact tests. This provides one verification of the present theory.

Substitution of Eq. (32) into Eq. (26) further yields

$$-\Delta\mathcal{K} = (C_0\Gamma^2\rho)^{1/3}\dot{\varepsilon}_D^{2/3} \quad \text{where } C_0 = C_k^3 C_a^2 \tag{35}$$

where $C_0 = 822$ for hexagonal prisms and $C_0 = 1013$ for cubical particles, assuming $H/h = 100$. Again the difference that results from different particle shapes is not large.

7. Dimensionless number separating fractures driven by kinetic and strain energies

What is the critical strain rate beyond which the fracturing driven by the release of kinetic energy of strain rate, $-\Delta\mathcal{K}$, dominates over the fracturing of classical type driven by the release of strain energy $\mathcal{U}$? To answer it, we must also include $\mathcal{U}$ in the energy balance. As is clear from Fig. 3, the domains of the particles to form are initially deformed by locally uniform shear strain $\gamma = 2\varepsilon_D$ and after comminution fracture they become undeformed. So the strain energy release due to comminution fracture is $\mathcal{U} = \tau^2/2G$ where G is the elastic shear modulus and τ is the shear stress. According to Eq. (35), we have

$$-\frac{\Delta\mathcal{K}}{\mathcal{U}} = B_a \tag{36}$$

$$B_a = \frac{G}{C_g\tau^2}(\Gamma^2\rho\dot{\varepsilon}_D^2)^{1/3} \tag{37}$$

$$\text{where} \quad C_g = C_0^{-1/3}/2 = 1/(2C_kC_a^{2/3}) = 0.2656 \text{ for } H/h = 10 \tag{38}$$

where C_g is a dimensionless geometry factor depending on the particle shape and the type of frequency distribution of particle sizes. For $H/h = 10$ and for the hexagonal particles distributed according the Schuhmann law, $C_g = 0.2656$. For other shapes, distributions and ratios H/h, different values will be obtained but they will generally be of the order of 1. B_a is a dimensionless number, an indicator of the onset of comminution, characterizing the importance of kinetic shear fracturing in the comminution process. The comminution is

$$\begin{aligned} &\text{kinetic energy driven if} \quad B_a \gg 1 \\ &\quad \text{in transition if} \quad B_a \approx 1 \\ &\quad \text{absent or static if} \quad B_a \ll 1 \end{aligned} \tag{39}$$

Since τ at comminution cannot be larger than the shear strength or yield stress τ_0, the use of $\tau = \tau_0$ in the condition $B_a \gg 1$ gives a sufficient condition for comminution to be driven by the kinetic energy alone.

In the flow of fluids, the dimensionless Reynolds number gives the threshold beyond which the local kinetic energy due to eddies begins to control the resistance to flow. Likewise, B_a is a dimensionless number that defines the threshold beyond which the local kinetic energy due to shear strain rate begins to control the resistance to deformation. This is another feature of the turbulence analogy.

Expressing $\dot{\varepsilon}_D$ from Eq. (32) and substituting it into (37), one gets an alternative expression for the dimensionless indicator:

$$B_a = \frac{C_a^{1/3}}{C_g}\,\frac{G\Gamma}{\tau_0^2 h} \tag{40}$$

8. Some numerical estimates and discussion

Let us now estimate the dimensionless number B_a for shear comminution of concrete. While, at the macroscale, the fracture energy of concrete is about 100 J/m^2, for sub-millimeter particles it is probably much smaller, perhaps $\Gamma = 10$ J/m^2 $= 10$ kg/s^2, because the fracture process zone is much narrower. Further we may consider $\tau_0 = 3$ MPa $= 3\times 10^6$ kg s^{-2} m^{-1}, $G = 10.59$ GPa $= 10.59 \times 10^9$ kg s^{-2} m^{-1}, and $\rho = 2300$ kg/m^3. Assuming $H/h = 10$ and $H = 9.43$ mm (or $\dot{\varepsilon}_D = 100$ s^{-1}), we have $B_a = 5.85$. Considering the strain rates $\dot{\varepsilon}_D = 10^4$/s and 10^6/s, we get from Eq. (36):

$$-\frac{\Delta\mathcal{K}}{\mathcal{U}} = 126 \quad \text{and } 2715 \tag{41}$$

respectively. So, at these rates, the deformation is almost totally dominated by the kinetic energy of strain rate. In a similar way, one finds that

$$-\Delta\mathcal{K}/\delta\mathcal{U} = 1 \quad \text{when } \dot{\varepsilon} = 7.075/\text{s}. \tag{42}$$

Since the values of Γ and τ_0 at sub-millimeter scale are highly uncertain, the foregoing estimates must, of course, be regarded as very crude. It is better to calibrate the computational model by fitting impact test data.

Let us now estimate the particle size. We assume the same values of Γ and ρ as before and (for $\dot{\varepsilon}_D = 10^4\ \mathrm{s}^{-1}$, $H/h = 10$ and $k = 0.5$) we calculate $C_a = 1.929$. From Eq. (32) with (33), we get the minimum and mean particle sizes:

$$h = 0.4377\ \text{mm for } \dot{\varepsilon}_D = 10^4/\text{s}, \quad h = 0.0943\ \text{mm for } \dot{\varepsilon}_D = 10^5/\text{s} \tag{43}$$

$$\bar{s} = 2.066\ \text{mm for } \dot{\varepsilon}_D = 10^4/\text{s}, \quad \bar{s} = 0.4452\ \text{mm for } \dot{\varepsilon}_D = 10^5/\text{s} \tag{44}$$

Under high confining hydrostatic pressure p, say $p = 10\tau_0$, the effective fracture energy might increase significantly. This would increase the foregoing estimates of threshold and particle size. But under high enough pressure the material would behave plastically and would not comminute.

Another point to note is that the release of strain energy $\mathcal{U}$ does not lead to dependence of fracturing on the strain rate. Rather, it leads to a dependence on the magnitude of applied stress or strain, which is already accounted for by the softening part of the constitutive relation.

9. Implementation of kinetic rate effect

Energy conservation requires that $\mathcal{K} = \mathcal{D} =$ energy dissipated per unit volume (dimension J/m^3). As the same time, since the stress (dimension N/m^2) is the energy per unit volume, $\Delta\mathcal{K} = \sigma^A =$ additional stress due to comminution. There are two possible approaches to enforce this energy dissipation in a finite element program:

(1) Either as a distributed body force

$$\boldsymbol{f} = \partial\mathcal{K}/\partial\boldsymbol{x} \quad (\Delta\mathcal{K} = \mathcal{D} = \sigma^A) \tag{45}$$

which gets translated into equivalent nodal forces ($\boldsymbol{x}$ = global coordinate vector formed from Cartesian coordinates x_i, $i = 1, 2, 3$);

(2) Or as an additional stress, $\sigma^A = \mathcal{D}$, to be implemented in the constitutive equation. We favor this approach as it seems simpler for programming, and also is more versatile as it allows generalization to different types of comminution.

Since one may write $\sigma^A = \mathcal{D} = \eta\dot{\varepsilon}$, the additional (apparent) viscous stress σ^A may be implemented as kinetic (or apparent) viscosity $\eta = \mathcal{D}/\dot{\varepsilon} = -\Delta\mathcal{K}/\dot{\varepsilon}$. But this equation would be acceptable only in a uniaxial model. In a triaxial constitutive model, the additional viscous stress should be applied only to the stress components that represent shear, i.e., as additional deviatoric stress components s_{ij}^A, which must be added to the stresses obtained from the standard quasi-static constitutive model.

To ensure tensorial invariance, powers of the tensorial components are inadmissible. Only a tensorial invariant can be raised to a power. So we use again the effective deviatoric strain rate given by Eq. (5). Since the energy density has the same dimension as the stress, it is convenient to introduce equivalent viscosity η_D such that the viscous stress–strain relation

$$s_{ij}^A = \eta_D \dot{\varepsilon}_{D\,ij} \tag{46}$$

where

$$\eta_D = (C_0 \Gamma^{-2} \rho)^{1/3} \dot{\varepsilon}_D^{\,-1/3} \tag{47}$$

would give the same energy dissipation density as Eq. (35) for any possible deviatoric strain rate tensor $\dot{\varepsilon}_{D\,ij}$, in the variational sense. Now, because the energy density is the same as the stress, s_{12}^A must be equal to $\Delta\mathcal{K}$ when all other tensorial components vanish. Since $\Delta\mathcal{K}$ is a tensorial invariant, it is thus necessary that

$$-\Delta\mathcal{K} = \sqrt{s_{ij}^A s_{ij}^A/2} \tag{48}$$

In view of Eq. (46), we may then write

$$\sqrt{s_{ij}^A s_{ij}^A/2} = \eta_D \sqrt{\dot{\varepsilon}_{D\,ij}\dot{\varepsilon}_{D\,ij}/2} = \eta_D \dot{\varepsilon}_D \tag{49}$$

where $\dot{\varepsilon}_D = \sqrt{\dot{\varepsilon}_{D\,ij}\dot{\varepsilon}_{D\,ij}/2}$. This is a tensorial invariant which simplifies to pure shear rate $\dot{\varepsilon}_D$ when $\dot{\varepsilon}_{D\,12}$ is the only nonzero component.

This analysis shows that the energy sink due to the comminution process may be modeled by equivalent apparent viscosity η_D. This is the simplest way to implement the comminution effect in finite element programs. It can be combined with any constitutive law.

The enhancement of the dissipative viscous resistance to shearing is a similar feature as the enhancement of viscous resistance caused by eddies in turbulent flow. This is another aspect of analogy with turbulence.

A stress increase proportional to $\dot{\varepsilon}^{2/3}$ gives an enormous rate effect on the apparent material strength, but only at very high strain rates. To illustrate this, consider that the strength or yield limit is scaled up by a rate-dependent factor, r, and note that, according to the test data in the literature, the rate effect beyond that explained by viscoelasticity and static crack growth rate is detectable only for rates $\dot{\varepsilon} > 1/\text{s}$. Knowing this fact suffices to estimate the rate effect magnitude. Assuming

that the error of the data is not below 1%, we have $1^{2/3}r = 0.01$, from which $r = 0.01$. So, e.g., at the strain rate of 10^5/s one has $(10^5)^{2/3}r = 21.5$. This is the ratio by which the stress must be increased, by means of apparent viscosity.

10. Generalization to kinetic energy of volume expansion and its apparent viscosity

In some situations, the rate of volumetric strain $\varepsilon_V = \varepsilon_{kk}/3$ can be so high that the volumetric kinetic energy is significantly contributing to the comminution (such a case was shown by Grady (1982, 1985) in his analysis of an explosion within a hollow sphere). In that case, Eqs. (6) need to be generalized as

$$\dot{u} = \dot{u}_0 - \dot{\omega}y + \dot{\varepsilon}_D y + \dot{\varepsilon}_{Ex}x, \quad \dot{v} = \dot{v}_0 + \dot{\omega}x + \dot{\varepsilon}_D x + \dot{\varepsilon}_{Ex}y \tag{50}$$

in which

$$\dot{\varepsilon}_{Ex} = \left\langle \frac{\mathrm{d}}{\mathrm{d}t}\left\langle \frac{\varepsilon_{kk}}{3}\right\rangle \right\rangle = \begin{cases} \dot{\varepsilon}_V & \text{if } \dot{\varepsilon}_V > 0 \text{ and } \varepsilon_V > 0 \\ 0 & \text{otherwise} \end{cases} \tag{51}$$

and t is the time, $\dot{\varepsilon}_{Ex}$ represents the expansive strain rate which is such that no comminution occurs if either the volumetric strain rate is compressive or if the volumetric strain is compressive (i.e., negative). Noting that Eq. (7) remains unchanged, one finds that Eqs. (26) and (35) for the drop of kinetic energy per unit volume of material must now be generalized as follows:

$$-\Delta\mathcal{K} = C_k\rho h^2(\dot{\varepsilon}_D^2 + \dot{\varepsilon}_{Ex}^2) \tag{52}$$

$$-\Delta\mathcal{K} = (C_0\Gamma^{-2}\rho)^{1/3}(\dot{\varepsilon}_D^2 + \dot{\varepsilon}_{Ex}^2)^{1/3} \tag{53}$$

This means that, in the remaining equations, $\dot{\varepsilon}_D^2$ must now be replaced by $\dot{\varepsilon}_D^2 + \dot{\varepsilon}_{Ex}^2$. Hence, Eq. (32) must be generalized as

$$h = s_{min} = \left(\frac{C_a\Gamma}{\rho(\dot{\varepsilon}_D^2 + \dot{\varepsilon}_{Ex}^2)}\right)^{1/3} \tag{54}$$

Eq. (46) must now be combined with the additional apparent tensile volumetric viscous stress, as follows:

$$s_{ij}^A = \eta_D\dot{e}_{ij}, \quad \sigma_V^A = \eta_V\dot{\varepsilon}_{Ex} \tag{55}$$

in which

$$\eta_V = (C_0\Gamma^2\rho)^{1/3}\ \dot{\varepsilon}_{Ex}^{-1/3} \tag{56}$$

here η_V is the volumetric kinetic (or apparent) viscosity.

Numerical simulations nevertheless show that the generalization for $\dot{\varepsilon}_{Ex}$ has virtually no effect in impact problems.

11. Static-to-kinetic transition of rate effect and apparent viscosity

Eq. (47) cannot be applied to very small loading rates, for two reasons: (1) numerical, because the viscosity would become infinite when $\dot{\varepsilon}_D \to 0$ and would thus cause the computer program to diverge if $\dot{\varepsilon}_D$ happens to be small enough and (2) physical, because the comminution by local kinetic energy does not exist according to Eq. (39) when $B_a \ll 1$. Thus, there must be a transition from finite to zero viscosity, centered at $B_a = 1$.

To deduce this transition, we must replace function $\dot{\varepsilon}_D^{-1/3}$ by a function that is asymptotically finite or zero when $\dot{\varepsilon}_D \to 0$ but remains asymptotically unchanged for high $\dot{\varepsilon}_D$. To this end, we express $\dot{\varepsilon}_D$ from Eq. (37) and substitute it into Eq. (47) to express the viscosity in terms of B_a:

$$\eta_D = \frac{\Gamma}{\tau_0}\left(\frac{C_0^{2/3}G_\rho}{C_g B_a}\right)^{1/2} \tag{57}$$

This equation may now be replaced by the following:

$$\eta_D = \frac{\Gamma}{\tau_0}\left(\frac{C_0^{2/3}G_\rho}{C_g}\,\frac{B_a^{n-1}}{1+B_a^n}\right)^{1/2} \tag{58}$$

where n is an empirical constant controlling how sharp the transition is; $n \geq 1$ (calculations used $n = 2$).

The foregoing equation is the final expression for the kinetic viscosity, with corrected low-rate asymptotics. It is identical to Eqs. (47) and (57) when $B_a \gg 1$ and gives a zero or negligible finite viscosity when $B_a \ll 1$, as required by (39).

12. Possible variability of Γ, work of friction and effect of pressure

When a high shear strain rate continues after the initial comminution by interface fracture, Γ plays the role of frictional work, i.e., the work of frictional shear stress τ on unit displacement. If $\dot{\varepsilon}_D$ after initial comminution decreases while still

remaining in the comminution range according to Eq. (37), the energy balance requires the frictional slip to be concentrated into interfaces spaced farther apart than particle size. Thus groups of particles moving as virtually rigid blocks must form and Γ then represents the work of friction between these blocks. On the other hand, if the shear strain rate after the initial comminution increases further, the particles already comminuted must be getting comminuted further (or fractured) to smaller sizes.

Since friction decreases with increasing slip rate, the frictional work may be decreasing with increasing strain rate. This effect could be approximately captured by setting

$$\Gamma \propto \dot{\varepsilon}_D^{-q} \quad (q \geq 0) \tag{59}$$

However, to verify such an effect and determine the value of q, further more detailed test data will be necessary. In data fitting thus far, the possible effect of $\dot{\varepsilon}$ on Γ has been neglected.

Note that exponent $-1/3$ in Eq. (47) has been derived for constant Γ. However, if Γ as a characteristic of post-fracture frictional work decreases with the slip rate or shear strain rate according to the power law in Eq. (59), it would reduce the exponent in Eq. (47) below $-1/3$. However, the particle size given by Eq. (32) would not be affected since it depends on the fracture energy rather than the subsequent frictional slip.

When the high-rate shearing occurs under high hydrostatic pressure p, the effective value of Γ in the sense of fracture energy as well as frictional work may increase as a function of p.

It may be noted that a different fracture energy and particle size effects have been observed in the case of dynamic erosion of a solid surface by impinging hard particles (Tilly and Sage, 1970). However, this is a fundamentally different problem to which the present theory does not apply.

13. Conclusions

1. The local kinetic energy of motion associated with high shear strain rates ($>10^2$/s) is sufficient to provide the surface fracture energy necessary for comminution of materials such as concrete into fine particle.
2. At very high strain rates, kinetic energy of strain rate is orders of magnitude higher than the strain energy. Hence, the classical fracture mechanics does not apply.
3. The dissipated energy depends on the particle size distribution, which is here assumed to follow the Schuhmann power law.
4. The minimum or average particle size follows from the condition that the rate of release of kinetic energy of shear strain rate must be equal to the rate of energy dissipation due to growing area of interparticle fractures. The minimum particle size predicted for missile impact at 310 m/s is of the order of 0.15 mm.
5. The main characteristic of the comminution effect is a dimensionless number B_a (Eq. (37)) representing the ratio of local kinetic energy of shear strain rate to the maximum possible strain energy that can be stored in the same volume of material.
6. The present theory indicates that the density of kinetic energy available for comminution is proportional to the (2/3) power of the shear strain rate, the particle size or crack spacing is proportional to the $(-2/3)$ power of that rate, and the energy dissipation by comminution is equivalent to a shear viscosity decreasing as the $(-1/3)$ power of that rate. For a strain rate increase from 1/s to 10^5/s, the result is a roughly 20-fold increase of apparent material strength due to comminution.
7. After comminution, the role of interface fracture energy changes to the work of interface frictional slip per unit relative displacement. If the interface friction depends on the slip rate, the exponent of strain rate giving the effective viscosity can change.
8. As one experimental justification, the present theory agrees with Grady's empirical observation that, in impact events, the average particle size is inversely proportional to the (2/3) power of the shear strain rate (Eq. (1)).
9. The theory can be extended in a similar way by including particle comminution due to kinetic energy of volumetric strain rate, although, for missile impact, the volume expansion is not important.
10. The theory leads to a rate-dependent modification of constitutive equation calibrated only for static strain rate effects.

Acknowledgments

The initial microplane modeling was supported under Grant W911NF-09-1-0043/P00003 from the U.S. Army Research Office, Durham, to Northwestern University. The modeling of comminution due to local kinetic energy of strain rate was supported by the Agency for Defense Development (ADD), Korea, through Grant 32788 from Daejeon University to Northwestern University.

Appendix A. The alternative of increasing strength or yield limit

Since the energy per unit volume (dimension J/m^3, with J=N m) has the same dimension as the stress (dimension N/m^2), an increase in the strain rate may alternatively be considered to cause an increase in the strength or yield limit in the constitutive law. In the microplane model, the compressive deviatoric boundary curve for deviatoric stress σ_D, and the normal boundary for tensile normal stress σ_N, respectively, may thus be scaled up by the kinetic factors:

$$r_D = (C_D l^2 \rho)^{1/3} \langle \dot{\varepsilon}_D \rangle^{2/3}, \quad r_V = (C_V l^2 \rho)^{1/3} \langle \dot{\varepsilon}_N \rangle^{2/3} \tag{A.1}$$

where ε_D is now the microplane deviatoric strain component, ε_N the microplane normal strain component, and C_V, C_D microplane stiffness constants.

Modeling of the enhanced resistance to high-velocity missile penetration by raising of the boundaries on the microplanes was attempted by Adley et al. (2012) and Frank et al. (2012). They raised the boundaries purely empirically, in a way that allowed them to fit their missile penetration data.

However, in the microplane model there are many boundaries and each has a different and complicated shape controlling the triaxial behavior. Thus different boundaries and different parts of each boundary would have to be raised by different ratios, which would reshape the boundaries. Unfortunately, it appears to be next to impossible to do that without loosing the foundation of the microplane model in the static triaxial test data. This is a serious objection to this kind of empirical approach.

References

Adley, M.D., Frank, A.O., Danielson, K.T., 2012. The high-rate brittle microplane concrete model: part I: bounding curves and quasi-static fit to material property data. Comput. Concr. 9, 293–310.

Bažant, Z.P., Caner, F.C., 2013. Comminution of solids caused by kinetic energy of high shear strain rate, with implications for impact, shock, and shale fracturing. Proc. Natl. Acad. Sci. 110 (48), 19291–19294.

Bažant, Z.P., Caner, F.C., Adley, M.D., A, A.S., 2000. Fracturing rate effect and creep in microplane model for dynamics. ASCE J. Eng. Mech. 126, 962–970.

Bažant, Z.P., Le, J.L., Greening, F.R., Benson, D.B., 2008. What did and did not cause collapse of World Trade Center twin towers in New York? ASCE J. Eng. Mech. 134, 892–906.

Bažant, Z.P., Lin, F.B., 1988. Nonlocal smeared cracking model for concrete fracture. ASCE J. Struct. Eng. 114, 2493–2510.

Cadoni, E., Labibes, K., Albertini, C., Berra, M., Giangrasso, M., 2001. Strain-rate effect on the tensile behaviour of concrete at different relative humidity levels. Mater. Struct. 34 (January–February), 21–26 (RILEM, Paris).

Camacho, G.T., Ortiz, M., 1996. Computational modelling of impact damage in brittle materials. Int. J. Solids Struct. 33, 2899–2938.

Caner, F.C., Bažant, Z.P. Impact comminution of solids due to local kinetic energy of high shear strain rate: II. Microplane model and verification. J. Mech. Phys. Solids, http://dx.doi.org/10.1016/j.jmps.2013.11.009, this issue.

Caner, F.C., Bažant, Z.P., 2013. Microplane model M7 for plain concrete: I. Formulation. ASCE J. Eng. Mech. 139, 1714–1723.

Caner, F.C., Bažant, Z.P., Wendner, R., 2013. Microplane model M7f for fiber reinforced concrete. Eng. Fract. Mech. 105, 41–57.

Charles, R.J., 1957. Energy-size reduction relationships in comminution. Min. Eng. 9, 80–88.

Cunningham, C., 1987. Fragmentation estimation and the Kuz–Ram model—four years on. In: Fourney, W.L., Dick, R.D. (Eds.), Proceedings of the Second International Symposium on Rock Fragmentation by Blasting, SEM, Bethel, Connecticut, pp. 475–487.

Deshpande, V.S., Evans, A.G., 2008. Inelastic deformation and energy dissipation in ceramics: a mechanism-based constitutive model. J. Mech. Phys. Solids 56, 3077–3100.

Doyoyo, M., 2002. A theory of the densification-induced fragmentation in glasses and ceramics under dynamic compression. Int. J. Solids Struct. 39, 1833–1843.

Ferri, E., Deshpande, V., Evans, A., 2010. The dynamic strength of a representative double layer prismatic core: a combined experimental, numerical, and analytical assessment. ASME J. Appl. Mech. 77. 061011-1–061011-7.

Forquin, P., Gary, G., Gatuingt, F., 2008. A testing technique for concrete under confinement at high rates of strain. Int. J. Impact Eng. 35, 425–446.

Frank, A.O., Adley, M.D., Danielson, K.T., McDevitt, H.S., 2012. The high-rate brittle microplane concrete model: part II: application to projectile perforation of concrete. Comput. Concr. 9, 311–325.

Freund, L., 1990. Dynamic Fracture Mechanics. Cambridge University Press, Cambridge, UK.

Gailly, B., Espinosa, H., 2002. Modelling of failure mode transition in ballistic penetration with a continuum model describing microcracking and flow of pulverized media. Int. J. Numer. Methods Eng. 54, 365–398.

Gao, H., Klein, P., 1998. Numerical simulation of crack growth in an isotropic solid with randomized internal cohesive bonds. J. Mech. Phys. Solids 46, 187–218.

Gatuingt, F., Pijaudier-Cabot, G., 2002. Coupled damage and plasticity modelling in transient dynamic analysis of concrete. Int. J. Numer. Anal. Methods Geomech. 26, 1–24.

Grady, D.E., 1982. Local inertial effects in dynamic fragmentation. J. Appl. Phys. 53, 322–325.

Grady, D.E., 1985. The mechanics of fracture under high-rate stress loading. In: Bažant, Z.P. (Ed.), Mechanics of Geomaterials. John Wiley, Chichester, UK, pp. 129–156. (Chapter 7).

Grady, D.E., 1990. Particle size statistics in dynamic fragmentation. J. Appl. Phys. 68, 6099–6105.

Grady, D.E., 1998. Shock-wave compression of brittle solids. Mech. Mater. 29, 181–203.

Grady, D.E., 2010. Length scales and size distributions in dynamic fragmentation. Int. J. Fract. 163, 85–99.

Grady, D.E., Kipp, M.E., 1995. Experimental measurement of dynamic failure and fragmentation properties of metals. Int. J. Solids Struct. 32, 2779–2991.

Grady, T.E., Kipp, M.E., 1979. The micromechanics of impact fracture of rock. Int. J. Rock Mech. Min. Sci. 16, 293–302.

Jirásek, M., Bažant, Z.P., 1995. Particle model for quasibrittle fracture and application to sea ice. ASCE J. Eng. Mech. 121, 1016–1025.

Kipp, M.E., Grady, D.E., Chen, E.P., 1980. Strain-rate dependent fracture initiation. Int. J. Fract. 16, 471–478.

Klein, P., Gao, H., 1998. Crack nucleation and growth as strain localization in a virtual-bond continuum. Eng. Fract. Mech. 61, 21–48.

Kožar, I., Ožbolt, J., 2010. Some aspects of load-rate sensitivity in visco-elastic microplane material model. Comput. Struct. 7, 317–329.

Mescall, J., Weiss, V., 1984. Materials behavior under high stress and ultrahigh loading rates—part II. In: Proceedings of the 29th Sagamore Army Conference, Army Materials and Mechanics Research Center, Watertown, Massachusetts.

Mott, N.F., 1947. Fragmentation of shell cases. Proc. Roy. Soc. A 189, 300–308.

Ouchterlony, F., 2005. The Swebrec function: linking fragmentation by blasting and crushing. Min. Technol. 114, A29–A44.

Ožbolt, J., Sharma, A., Reinhardt, H.W., 2011. Dynamic fracture of concrete—compact tension specimen. Int. J. Solids Struct. 48, 1534–1543.

Reinhardt, H.W., Weerheijm, J., 1991. Tensile fracture of concrete at high loading rates taking account of inertia and crack velocity effects. Int. J. Fract. 51, 31–42.
Schuhmann, R.J., 1940. Principles of Comminution, I. Size Distribution and Surface Calculation. Technical Report. The American Institute of Mining, Metallurgical, and Petroleum Engineers (AIME).
Shih, C.J., Nesterenko, V.F., Meyers, M.A., 1998. High-strain-rate deformation and comminution of silicon carbide. J. Appl. Phys. 83, 4660–4671.
Tennekes, H., Lumley, J.L., 1972. A First Course in Turbulence. MIT Press, Cambridge, MA.
Tilly, G.P., Sage, W., 1970. The interaction of particle and material behavior in erosion processes. Wear 16, 447–465.
Wei, Z., Evans, A.G., Deshpande, V.S., 2009. The influence of material properties and confinement on the dynamic penetration of alumina by hard spheres. ASME J. Appl. Mech. 76. 051305-1–051305-8.

Journal of the Mechanics and Physics of Solids 67 (2014) 14

Contents lists available at ScienceDirect

Journal of the Mechanics and Physics of Solids

journal homepage: www.elsevier.com/locate/jmps

Corrigendum

Corrigendum to Impact comminution of solids due to local kinetic energy of high shear strain rate: I. Continuum theory and turbulence analogy [J. Mech. Phys. Solids 64 (2014) 223–235]

Zdeněk P. Bažant [a,b,*], Ferhun C. Caner [a,b]

[a] Northwestern University, 2145 Sheridan Road, CEE/A135, Evanston, IL 60208, United States
[b] Institute of Energy Technologies, Technical University of Catalonia, Av. Diagonal 647, 08028 Barcelona, Spain

The authors regret that the following figure was not included. This figure should have been included on p. 6 as Fig. 4, with the remaining figure numbers sequentially updated.

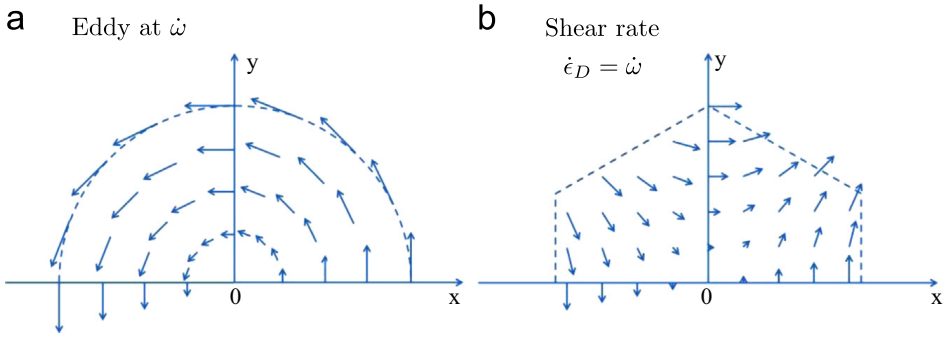

Fig. 4. Velocity vector fields of (a) idealized eddy rotating as a rigid body at angular velocity $\dot{\omega}$, and (b) pure shear. For deviatoric strain rate $\dot{\epsilon}_D = \dot{\omega}$, both fields have the same kinetic energy for the same area.

Furthermore, the authors regret a numerical error in Eq. (2) which affected values of several parameters, as follows:

Eq. (12) should read $I_p = 5\sqrt{3}/128\, h^4 \doteq 0.06766\, h^4$, $c_k = I_p/2hV_p \doteq 0.05208$. The correction in I_p requires the following corrections of the numerical values of various dimensionless constants throughout the paper: In the paragraph following Eq. (27), $C_k = 115.7$, 185.2. In Eqs. (30) and (31), replace ΔK by $|\Delta K|$. In the paragraph that follows Eq. (33), $C_a = 0.026$ and $C_a = 0.015$. In the paragraph of Eq.(35), $C_0 = 1028$ and $C_0 = 1351$. In Eq. (38), C_g should be 0.2466. In the first paragraph of Section 8, $h = 8.75$ mm. In Eq. (41), $-\Delta K/U = 136$ and in Eq. (42), $\dot{\epsilon} = 6.325$/s. In Eq. (43), change 0.4377 mm to 0.4063 mm and 0.0943 mm to 0.0875 mm. In the paragraph of Eq. (43), $C_a = 1.543$. In Eq. (44), change 2.066 mm to 1.918 mm and 0.4452 mm to 0.4133 mm. In Fig. 3a, change distance label h to $h/2$. No change is needed in the data fits of part 2 because the parameters were scaled to fit thickest slab test.

DOI of original article: http://dx.doi.org/10.1016/j.jmps.2013.11.008
* Corresponding author at: Northwestern University, Civil Engineering and Materials Science, 2145 Sheridan Road, CEE/A135, Evanston, IL 60208, United States.
E-mail address: z-bazant@northwestern.edu (Z.P. Bažant).

http://dx.doi.org/10.1016/j.jmps.2014.03.001

Journal of the Mechanics and Physics of Solids 64 (2014) 236–248

Contents lists available at ScienceDirect

Journal of the Mechanics and Physics of Solids

journal homepage: www.elsevier.com/locate/jmps

Impact comminution of solids due to local kinetic energy of high shear strain rate: II—Microplane model and verification

Ferhun C. Caner [a,1], Zdeněk P. Bažant [b,*,2]

[a] Institute of Energy Technologies, Technical University of Catalonia, Av. Diagonal 647, 08028 Barcelona, Spain
[b] Northwestern University, 2145 Sheridan Road, CEE/A135, Evanston, IL 60208, United States

ARTICLE INFO

Article history:
Received 21 July 2013
Received in revised form
11 November 2013
Accepted 13 November 2013
Available online 26 November 2013

Keywords:
Fracture mechanics
Dynamic fracture
Comminution
Constitutive modelling
Concrete

ABSTRACT

The new theory presented in the preceding paper, which models the dynamic comminution of concrete due to very high shear strain rate, is now compared to recent test data on the penetration of projectiles through concrete walls of different thicknesses, ranging from 127 to 254 mm. These data are analyzed by an explicit finite element code using the new microplane constitutive model M7 for concrete, which was previously shown to provide the most realistic description of the quasi-static uni-, bi- and tri-axial test data with complex loading path and unloading. Model M7 incorporates the quasi-static strain rate effects due viscoelasticity and to the rate of cohesive crack debonding based on activation energy of bond ruptures, which are expected to extend to very high rates. Here model M7 is further enhanced by apparent viscosity capturing the energy dissipation due to the strain-rate effect of comminution. The maximum shear strain rates in the computations are of the order of $10^5\ s^{-1}$. The simulations document that, within the inevitable uncertainties, the measured exit velocities of the projectiles can be matched quite satisfactorily and the observed shapes of the entry and exit craters can be reproduced correctly.

1. Introduction

The preceding Part 1 (Bažant and Caner, this issue) presented a new theory that allows the energy dissipation due to dynamic comminution of material under impact to be modeled through the constitutive relation which can be readily implemented in standard finite element programs. The comminution is assumed to be driven by the release of local kinetic energy of high shear strain rate caused by impact, and the energy dissipation due to comminution and inter-particle slip is modeled by additional apparent viscosity.

In the present part 2, the theory is being applied to the problem of penetration of missiles through concrete walls of various thicknesses. Fitting of previously published impact test data is used to calibrate and validate the new theory.

Because of the complexity of triaxial softening damage in concrete, the microplane model is selected as the constitutive law, to be enriched by the comminution rate effect. The microplane model has already been used with great success for the simulations of various dynamic effects on hardened concrete structures, including the effects of explosions, impact and

* Corresponding author. Tel.: +1 847 491 4025; fax: +1 847 491 4011.
E-mail addresses: ferhun.caner@upc.edu (F.C. Caner), z-bazant@northwestern.edu (Z.P. Bažant).
[1] Associate Professor at the Institute of Energy Technologies, Technical University of Catalonia and Visiting Scholar at Dept. of Civil and Env. Engineering, Northwestern University.
[2] McCormick Institute Professor and W.P. Murphy Professor of Civil Engineering and Materials Science.

0022-5096/$ - see front matter © 2014 Published by Elsevier Ltd.
http://dx.doi.org/10.1016/j.jmps.2013.11.009

groundshock. In contrast to plastic and other tensorial constitutive models, various microplane models have been shown capable of predicting the correct entry and exit crater shapes of penetrating missiles (Bažant et al., 2000a; Adley et al., 2012).

However, prediction of the exit velocities of perforating projectiles proved to be much more challenging. Recently a new model based on the microplane model M4, called the high-rate brittle microplane model, has been developed at U.S. Army Corps of Engineers (Adley et al., 2012). To fit the exit velocities, the microplane stress–strain boundaries (i.e., strain-dependent yield limits) were scaled up drastically, both vertically and horizontally, as functions of the strain rate (Adley et al., 2012). But the scaling ratios were empirical, with no theory behind them. Their empirical nature unfortunately severed the connection to the numerous types of static uni-, bi-, and tri-axial tests by which M4 was calibrated. Besides, in the sense of crack-band or nonlocal concept, the model in Adley et al. (2012) implied a major increase of fracture energy, while the previous studies showed the fracture energy to be only weakly dependent on the strain rate. This study will show that an extended microplane model, labeled M7R, which incorporates the theory of material comminution expounded in Part I, can fit the exit velocities satisfactorily without loosing the capability to fit all the static tests.

2. Review of microplane model and its version M7

The internal friction in materials is usually modeled as a relation between the first stress invariant and the second deviator invariant, without any reference to the direction of slip. This is not realistic. The plastic or frictional slip occurs in fact only on planes of a certain specific orientation. Likewise, almost all of the other inelastic deformations in concrete microstructure, such as tensile cracking and compressive axial splitting, occur on planes of well defined orientations. These orientations can be captured by the idea of Taylor (1938) who proposed to formulate the constitutive law in terms of the vectors of stress and strain acting on planes of various orientations in the material. This idea was first developed for plasticity of polycrystalline metals under the name of slip theory of plasticity (Batdorf and Budianski, 1949) and has by now led to powerful plasticity models called the Taylor models (Butler and McDowell, 1998; Rice, 1971). In these models, the stress vectors on the slip planes are the projections of the continuum stress tensor, which is called the static constraint, and the plastic slips on all the slip planes are simply superposed.

In the early 1980s, it was realized (Bažant, 1984; Bažant and Oh, 1985) that Taylor models are unstable in the case of strain-softening damage due to diffuse microcracking. To ensure model stability, the static constraint had to be changed to the kinematic constraint, in which the strain vector is the projection of the strain tensor onto a generic plane in the microstructure, called the microplane. Also the elastic deformation had to be included on the microplane level. The static equivalence of the stress tensor with stress vectors on microplanes of all possible spatial orientations was enforced by the principle of virtual work, which gives the continuum stress tensor

$$\sigma_{ij} = \frac{3}{2\pi}\int_{\Omega}(\sigma_N N_{ij} + \sigma_L L_{ij} + \sigma_M M_{ij})\,\mathrm{d}\Omega \tag{1}$$

This is an integral over a unit hemisphere Ω, in which σ_{ij}=stress tensor, $\sigma_N, \sigma_L, \sigma_M$ = normal and two shear components of the microplane stress vector, and N_{ij}, L_{ij}, M_{ij} = geometrical coefficients defined later. This integral is evaluated approximately according to an optimum Gaussian integration formula as a weighted sum over all the discrete microplanes whose normals are chosen to correspond to the integration points of this formula.

Compared to the classical tensorial constitutive models based on tensorial invariants, the microplane concept has a number of advantages: (1) It is conceptually simpler, since the strain vectors on the microplanes can be intuitively related to crack opening and slip. (2) The orientation of cracking and slip can be captured. (3) The so-called vertex effect is automatic, while being beyond the capability of the tensorial constitutive models. (4) Apparent deviations from normality in the sense of tensorial plasticity models are represented, thanks to the fact that the microplane model is equivalent to a large set of simultaneously active yield surfaces intersecting at the same point of the stress space, for each of which the normality rule can be satisfied (this is particularly important for dynamic loading, with highly nonproportional loading paths). (5) The kinematic constraint of the microplanes of different orientation automatically simulates the cross effects such as the shear dilatancy and pressure sensitivity. (6) Combinations of loading and unloading on different microplanes provide a complex path dependence and automatically reproduce the Bauschinger effect and the hysteresis under cyclic loading. (7) The dependence of the current yield or strength limits on the strain components (rather than on scalar hardening–softening parameters) is easy to take into account. (8) In cyclic loading, fatigue is automatically simulated by accumulation of residual stresses on the microplanes after each load cycle. (9) Finally, though not important for concrete, anisotropy can be easily captured.

Early on, the microplane model was computationally too demanding for full structures. But thanks to the rise of computer power, the microplane model is now being used in systems with tens of millions finite elements. Many progressively improved versions of the microplane model, now labeled M1, M2,…,M7, have been developed for concrete, and so have other variants for fiber-reinforced concrete, fiber–polymer composites, sandstone, shale, clay, rigid foam, shape memory alloy and some soft tissues. Model M4 (Bažant et al., 2000b; Caner and Bažant, 2000) was used with success in large-scale simulation of various explosions and groundshock, and with partial success in missile impact and penetration of concrete walls. The new model M7 (Caner and Bažant, 2013a,b), used and refined in this work, brings about further significant improvements. It eliminates unrealistic lateral strains in postpeak tensile softening, gives damage dependent unloading and works even for cyclic loading with softening.

Let us now briefly review the basics of microplane formulation. According to the kinematic constraint, the normal component of the strain vector on a generic microplane of orientation defined by its unit normal n_i is

$$\varepsilon_N = n_i n_j \varepsilon_{ij} = N_{ij}\varepsilon_{ij} \tag{2}$$

where subscripts $i,j = 1,2,3$ refer to Cartesian coordinates x_i (Fig. 1). The in-plane shear strain vector on each microplane is represented by its two in-plane orthogonal components in the directions of unit in-plane coordinate vectors $\vec{m}$ and $\vec{l}$ which are generated randomly on each microplane. These components are (Bažant et al., 2000b; Bažant and Oh, 1985)

$$\varepsilon_M = \frac{1}{2}(n_i m_j + n_j m_i); \quad \varepsilon_{ij} = M_{ij}\varepsilon_{ij}; \quad \varepsilon_L = \frac{1}{2}(n_i l_j + n_j l_i)\varepsilon_{ij} = L_{ij}\varepsilon_{ij} \tag{3}$$

To be able to model the pressure-sensitive compressive behavior of concrete, it is necessary to split the microplane normal strains and stresses into their volumetric and deviatoric parts

$$\varepsilon_N = \varepsilon_V + \varepsilon_D; \quad \sigma_N = \sigma_V + \sigma_D \tag{4}$$

where $\varepsilon_V = \varepsilon_{kk}/3$ and $\varepsilon_D = (N_{ij} - \delta_{ij}/3)\varepsilon_{ij}$; σ_V and σ_D are computed from ε_V and ε_D by the microplane constitutive law. In contrast to previous microplane models, this split is in M7 introduced only for inelastic compressive behavior, and not for the elastic part of response nor inelastic tensile behavior.

The inelastic softening behavior is in microplane model best characterized by means of separate strength limits, or stress–strain boundaries, on the microplane stress components. Within the boundaries, the behavior is considered to be elastic, and it should be noted that in spite of that the macroscopic response represents the pre-peak nonlinearity because different microplanes enter the strain softening behavior at different moments of loading. The inelastic behavior, defined on the microplanes in terms of σ_N in tension and in terms of σ_V and σ_D in compression, can simply be specified as functions of the corresponding ε_N, ε_V and ε_D, while the shear stress components σ_M and σ_L are limited by boundaries depending on σ_N and ε_V.

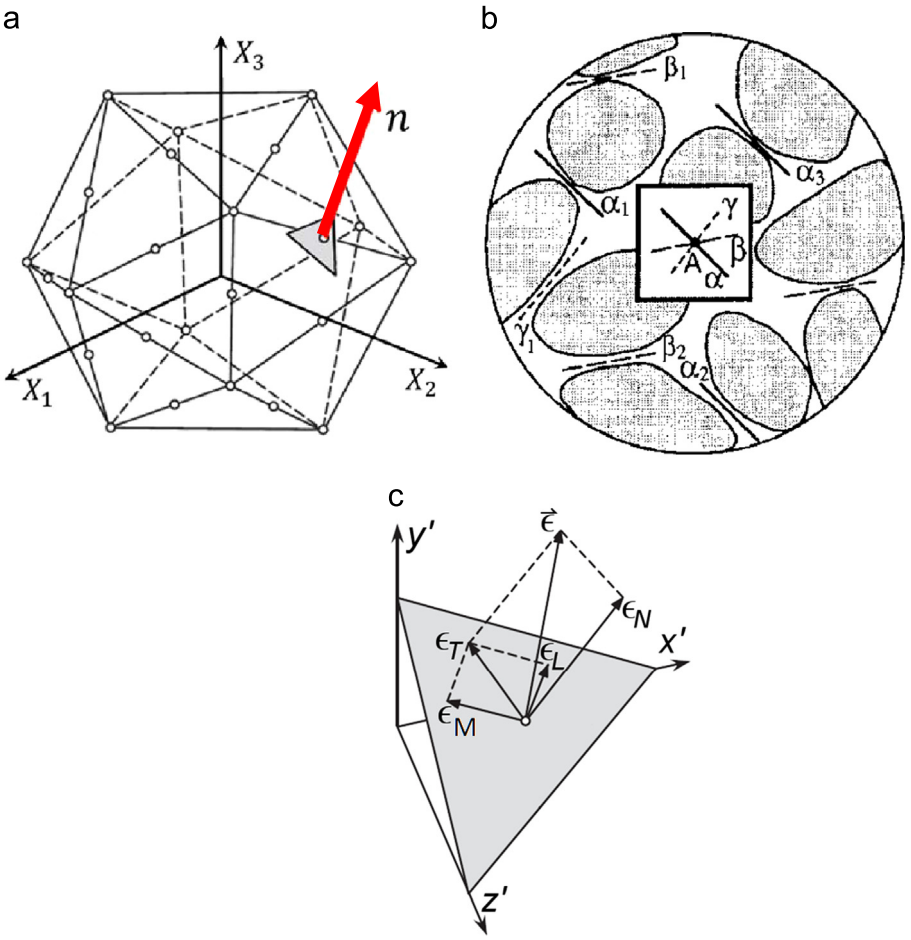

Fig. 1. (a) One Gauss point for each microplane and a typical normal at a microplane, (b) the concrete mesostructure with failure planes between aggregates modeled as microplanes, (c) the kinematic constraint giving rise to the microplane normal and shear strain components.

Accordingly, the tensile strength limit for normal microplane stresses, which governs tensile fracturing, can be defined as (see Fig. 2a and Eq. (23) in Caner and Bažant, 2013a)

$$\sigma_N^+ = \mathcal{F}_N(\varepsilon_N, \sigma_V) \tag{5}$$

The normal boundary, which governs the compressive failure, is given by

$$\sigma_N^- = \sigma_V + \sigma_D = \mathcal{F}_V(\varepsilon_V, \varepsilon_I, \varepsilon_{III}) + \mathcal{F}_D(\varepsilon_D, \varepsilon_V) \tag{6}$$

see Eqs. (13)–(14) and (16)–(18) in Caner and Bažant (2013a), and Fig. 2b and c, respectively; ε_I and ε_{III} are the maximum and minimum principal strains.

The microplane frictional yield surface is expressed as (see Fig. 2d and Eqs. (26)–(32) in Caner and Bažant, 2013a)

$$\sigma_\tau = \mathcal{F}_T(\varepsilon_\tau, \varepsilon_V, \sigma_N), \quad \varepsilon_\tau = \sqrt{\varepsilon_L^2 + \varepsilon_M^2}, \quad \sigma_\tau = \sqrt{\sigma_L^2 + \sigma_M^2} \tag{7}$$

Based on extensive calibrations by test data for many concretes, the stress–strain boundaries are in M7 characterized by five free parameters k_i ($i=1, 2,\ldots,5$), which can be easily adjusted according to basic data from uniaxial and triaxial compression tests and uniaxial tensile tests. Besides, the definitions of the boundaries include about twenty fixed parameters, which can be considered the same for all concretes. They have been identified by computer optimization of the fits of numerous data of different types. For details, see Caner and Bažant (2013a,b).

Based on the given elastic modulus E of concrete and given Poisson ratio ν, the kinematic constraint without volumetric–deviatoric split leads to the following values of the microplane normal and shear stiffness constants (Eq. (20a), (20b) in Bažant and Prat, 1988)

$$E_N = \frac{E}{1-2\nu}, \quad E_T = E_N \frac{1-4\nu}{1+\nu} \tag{8}$$

(also $E_N = K/3$ where K=bulk modulus). Obviously since both E_N and E_T must be non-negative, only Poisson's ratios in the range $\nu \in [-1, 0.25]$ can be reproduced. This range of ν is sufficient for concrete, for which $\nu \approx 0.18$. But it would not suffice

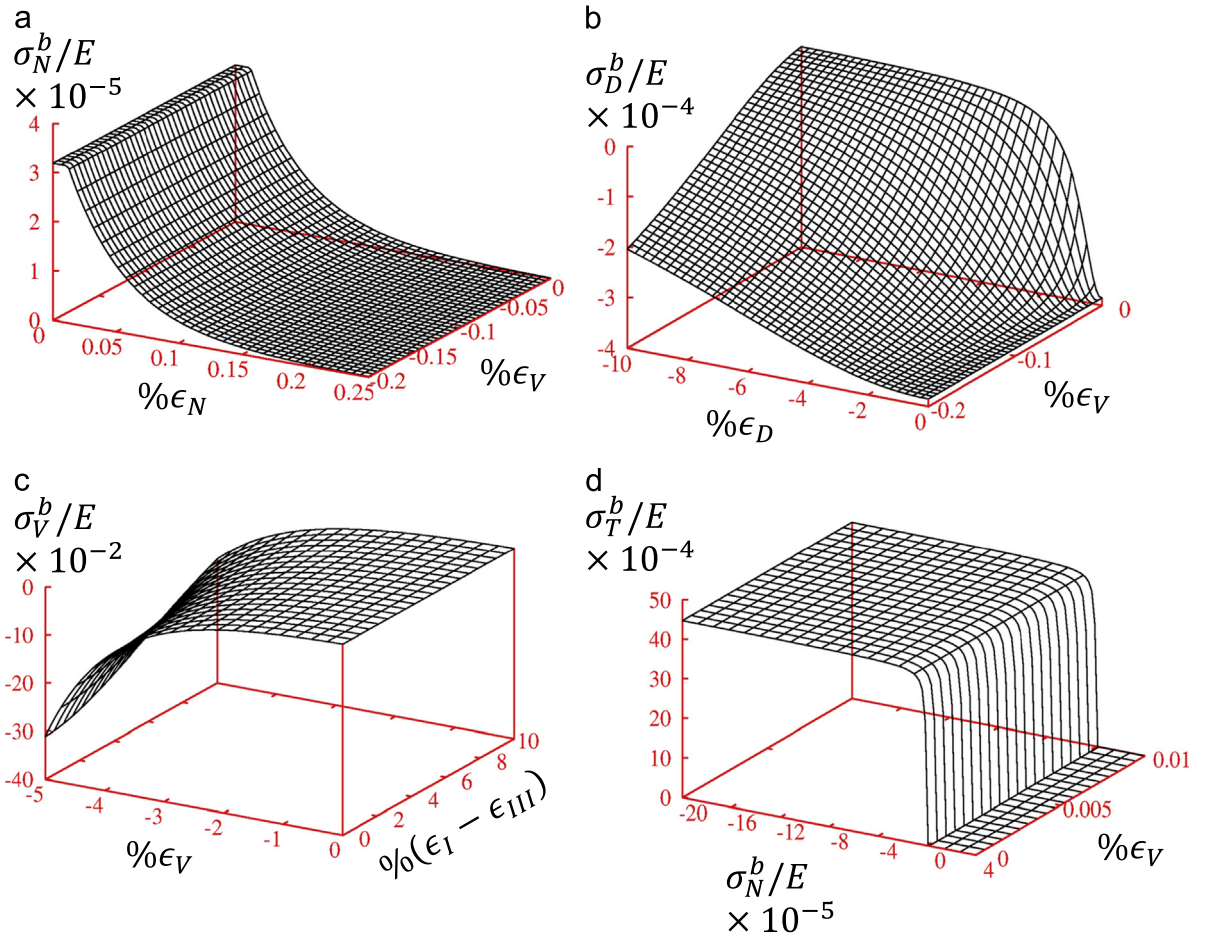

Fig. 2. (a) Microplane normal boundary, (b) microplane deviatoric boundary, (c) microplane volumetric boundary and (d) microplane frictional boundary.

for a general material, for which $\nu \in [-1, 0.5]$. In that case, to get the full range of ν, the microplane model M7 must be coupled in series with an isotropic shear-deformable elastic element of an infinite bulk modulus $K' = \infty$ and a finite shear modulus $G' > 0$ (Bažant and Oh, 1985) (see Fig. 2 in Caner and Bažant, 2013a; Caner et al., 2013).

The thermodynamic requirement of non-negative density of energy dissipation is discussed in detail in Caner and Bažant (2013a).

3. Calibration of model M7 by WES-5000 test data

Numerous earth penetration simulations in the literature have used the Eulerian coordinates, which are the coordinates of the current state and do not allow keeping the memory of the initial virgin state of the material. This approach is suitable for plastic materials. However, for brittle or quasibrittle materials, and particularly for the microplane model of concrete, memory of the initial virgin state is essential. Therefore, the updated Lagrangian approach, in which the material points are characterized by their coordinates in the initial state, must be used. Calculations show that the predicted geometry of the exit crater, as well as the deceleration of projectile prior to exit, depend strongly on the softening damage behavior of the material, whose characterization depends on the initial virgin state.

Given the complexity of concrete behavior, the constitutive law has been verified against a large set of experimental data covering virtually all the distinct types of experiments that characterize concrete, whose number is about 20 (Caner and Bažant, 2013b). A complicating feature of verification is that the test data used to verify Model M7 were obtained by numerous researchers in different laboratories, using different concretes. For calibration of model M7 for WES-5000 concrete, not only classical laboratory test data such as uniaxial and triaxial compression data, but also the test data obtained under unconventional loading paths (Cargile, 1999) have been employed, as shown in Fig. 3.

The same free model parameters, namely $E = 25$ GPa, $k_1 = 11 \times 10^{-5}$, $k_2 = 110$, $k_3 = 30$, $k_4 = 100$ and $k_5 = 1 \times 10^{-4}$, have been used for all the present data fits. Although in two cases the simulations show significant differences from the test data, the fit of a great majority of the simulations is good. Model M7 has also been verified by comparisons with the tests of compression–tension load cycles, the tests of mixed-mode crack propagation (see Figs. 4, 5, 6 and 7 in Caner and Bažant, 2013b), and the tests of explosions on plain concrete slabs.

The fits are performed by taking into account the meaning of the coefficients in terms of various particular aspects of the mechanical behavior of concrete. This kind of fitting procedure is more tedious than the automatic procedures such as the Levenberg–Marquardt optimization algorithm or the genetic algorithm but the resulting optimum values of the parameter preserve the robustness of the model in simulating general stress states. Complex automatic fitting procedures often yield parameter values that correspond to very close fits but almost always such parameter values render the model unstable in simulations of multiaxial states of stress. This is because it is not entirely possible to convey the meaning of each model parameter to the automatic fitting procedure.

4. Data from missile penetration tests

Slabs made of normal strength concrete, called the WES-5000 concrete, were perforated by projectiles at the Geotechnical and Structures Laboratory of the U.S. Army Engineer Research and Development Center (ERDC), Vicksburg (Frank et al., 2012). The slabs were circular, of thicknesses of 127, 216 and 254 mm, and were cast in steel culvert pipes of diameter of 1.52 m, two or three slabs for each thickness. The exit velocities were averaged. The projectiles had an ogive nose, weighed 2.3 kg and hit the slab with the entry velocity of 310 m/s and at an impact angle of 90° (with deviations of $< 1°$). The measured exit velocities of the projectiles were 225 m/s, 115 m/s and 45 m/s for the three slab thicknesses, respectively (Frank et al., 2012; Cargile, 1999). The geometries of the entry and exit craters were determined after the tests. Slabs of three different thicknesses were penetrated. As seen in finite element simulations, the strain rates in the thinnest slabs remained very high throughout the entire duration of the penetration. In the thickest slabs, the strain rates were very high initially but became only moderately high later on.

To obtain material data, standard cylindrical specimens of the same WES-5000 concrete were tested under both conventional and unconventional triaxial load paths (Caner and Bažant, 2000, 2013a). Frank et al. (2012). Various material models were calibrated with these quasistatic test data, and subsequently used to calculate the exit velocities as well as the entry and exit crater shapes in all three slabs. Despite using a variety of models, it turned out to be very challenging to match the test results (Frank et al., 2012).

5. Quasi-static rate effect in Model M7

As is clear from the preceding Part I (Bažant and Caner, this issue), there are two kinds of deformation rate effects—quasistatic and comminutive. The quasistatic rate effects are expected on theoretical grounds to extend to extreme rates and so they must be part of the material model even for such rates. Besides, even in projectile impact and perforation, the zones farther away from the missile are not deforming at extreme rates and exhibit only the quasistatic rate effects which play a role in wave attenuation and diffraction, and the same is true when the projectile forms the exit crater at greatly reduced velocity.

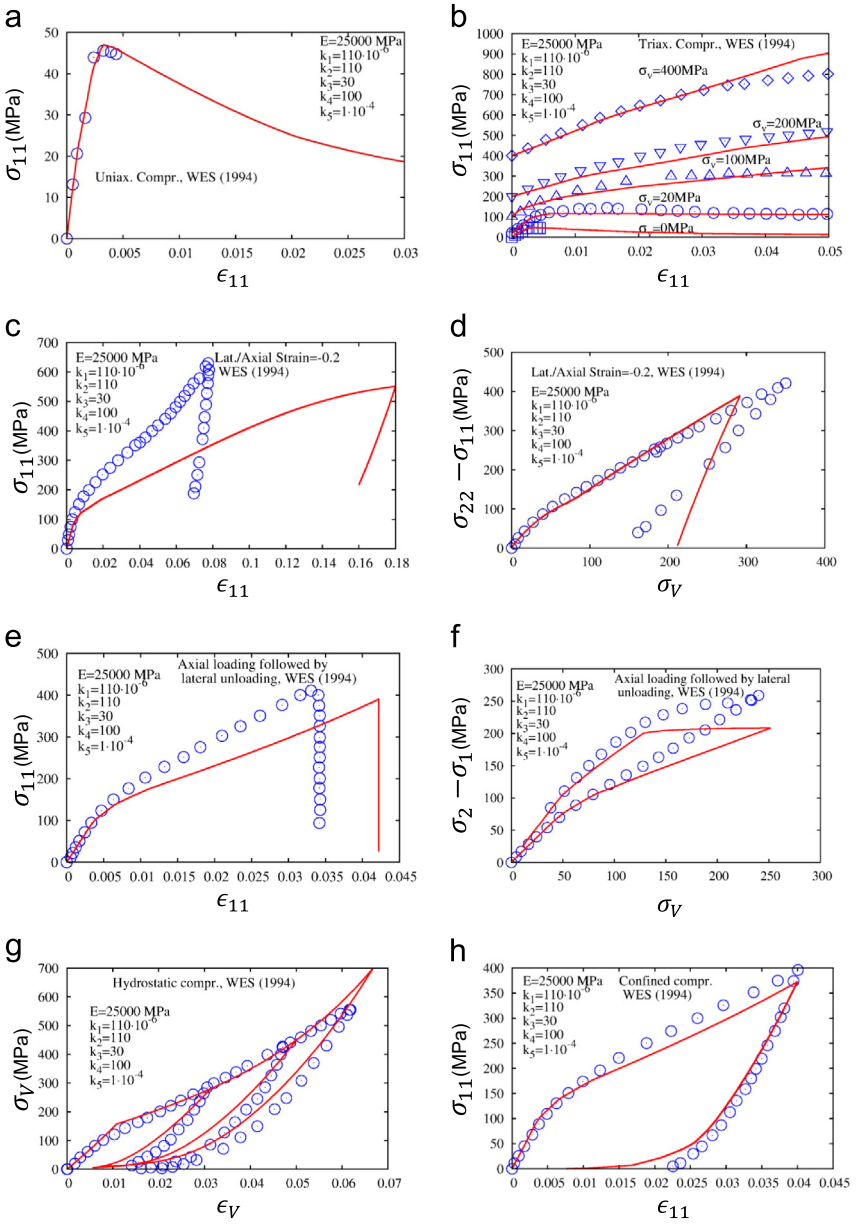

Fig. 3. Benchmark set of test data obtained with one and the same concrete, the WES-5000 concrete, used to evaluate the model and optimize material parameters.

Another way to generate rate effects in fracture modeling is through dynamic crack propagation and crack branching (e.g. Doyoyo, 2002). This approach has been pursued for metals and ceramics (see comments on the "Mescall" models in Part I). But it has not been elaborated for concrete and has not been developed in the form of a macro-continuum constitutive equation for finite element programs. In a general sense, though, the present comminution model and the dynamic crack branching are similar in that both simulate creation of small particles. The present model can in fact be regarded as an alternative to creation of a Mescall zone.

5.1. *Effect of cohesive crack separation rate*

One quasistatic rate effect, already introduced into microplane model M4 (Bažant et al., 2000a), is due to the rate dependence of cohesive crack opening w. It must follow the activation energy theory of bond ruptures. In this formulation, the rate dependence of the opening w of a cohesive crack (also called 'fictitious' crack) is described as (see Fig. 1a in Bažant

and Li, 1997 and Fig. 1 in Li and Bažant, 1997)

$$\dot{w} = k_0 \sinh\left(\frac{T_0}{T}\,\frac{\sigma - f^0(w)}{k_r N_b(w)}\right) e^{-(Q/k)(1/T - 1/T_0)} \tag{9}$$

where $\dot{w} = dw/dt$, t=time; σ=cohesive (crack-bridging) stress; k_0, k_r, T^0, Q, k = constants (k=Boltzmann constant; Q=activation energy of interatomic bond ruptures, T=absolute temperature; T_0=given reference temperature. and $N_b(w)$=number of surviving bonds spanning the cohesive crack, per unit area. Function $f^0(w)$ describes the softening law of the cohesive crack at an opening rate that is at the lower limit of the range of rates for which Eq. (9) is to be applied or has been calibrated (normally the rate of loading in static material tests in the laboratory). The adiabatic heating of concrete in an impact event has probably a negligible effect on $\dot{w}$, and in that case one may set $T \approx T_0$. Eq. (9) can be imagined to correspond to the rheologic model in which a rate-independent cohesive crack element is coupled in parallel with a nonlinear damper at each point of the cohesive crack (see Fig. 1b in Li and Bažant, 1997; Bažant et al., 2000a). The sinh-function in Eq. (9) ensues from the activation energy theory (rate-process theory, e.g. Krausz and Krausz, 1988) for bond ruptures.

The ratio $\sigma/N_b(w)$ represents the transmitted stress per bond, which is what matters for the activation energy theory. Obviously, N_b must decrease with increasing crack opening w and must drop to 0 when w becomes so large that $\sigma = f(w) = 0$. It has been assumed that

$$N_b(w) = C_b f^0(w) \tag{10}$$

where C_b is some proportionality constant.

The macroscopic strain softening may be imagined to be the result of the openings of many parallel cohesive cracks. Denoting by s_{cr} their average spacing, one may write

$$\dot{\varepsilon} = \frac{\dot{w}}{s_{cr}} + \frac{\dot{\sigma}}{E} \approx \frac{\dot{w}}{s_{cr}} \tag{11}$$

where ε=average macroscopic normal strain in the direction perpendicular to the parallel cracks, E=Young's modulus of uncracked material; $\dot{\sigma}/E$ represents the elastic strain rate, which is normally negligible by comparison if the crack is opening. It is by virtue of this observation that the approximation in Eq. (11) is justified.

Substituting $\dot{w} = s_{cr}\dot{\varepsilon}$ and Eq. (10) into Eq. (9) and solving the equation for σ, one obtains $\sigma = F(\varepsilon)$ where

$$F(\varepsilon) = \mathcal{F}(\varepsilon)\left[1 + C_2 \operatorname{asinh}\left(\frac{\dot{\varepsilon}}{C_1}\right)\right] \tag{12}$$

with

$$C_1 = C_0 e^{-(Q/R)(1/T - 1/T_0)}, \quad C_2 = C_r T/T_0, \quad \dot{\varepsilon} \geq 0 \tag{13}$$

Here $C_0 = k_0/s_{cr}$, $C_r = k_r C_b$ and $f^0(w) = \mathcal{F}(\varepsilon)$; C_0 and C_r are constants to be determined from tests. When the temperature is about the same as the temperature in the laboratory tests used for calibration, which is about 25 °C (T_0=298 K), then $C_1 = C_0$ and $C_2 = C_r$, and C_1 and C_2 become temperature independent, i.e., constants.

Since $\operatorname{asinh} x = \ln(x + \sqrt{x^2+1})$, the asymptotic approximation for $x^2 \gg 1$ is $\operatorname{asinh} x \approx \ln(2x)$. In Eq. (12), this occurs if the loading rate is so large that $\dot{\varepsilon}^2 \gg C_1$. Then Eq. (12) takes the form

$$F(\varepsilon) \approx \mathcal{F}(\varepsilon)\left[1 + C_2 \ln\left(\frac{2\dot{\varepsilon}}{C_1}\right)\right] \tag{14}$$

The logarithmic function is normally used for the rate effect on the yield limit in metal plasticity (e.g., in wavecode EPIC).

Function $F(\varepsilon)$ may be interpreted as the stress–strain boundary on the microplane corresponding to strain rate $\dot{\varepsilon}$, and $\mathcal{F}(\varepsilon)$ has the meaning of the static stress–strain boundary that corresponds to a vanishing strain rate (a boundary that approximately applies to the small loading rates of static material tests). The transformation from the static boundary $\mathcal{F}(\varepsilon)$ to the rate-dependent (dynamic) boundary represents, according to Eq. (12), a vertical scaling of the boundary curve (see Fig. 1c in Bažant et al., 2000a).

It is logical to assume that the normal and deviatoric boundaries adhere to Eq. (12). Thus, the following relations can be written on the microplane level:

$$F_N = \mathcal{F}_N[1 + c_{R2} R(\dot{\xi})] \tag{15}$$

$$F_D = \mathcal{F}_D[1 + c_{R2} R(\dot{\xi})] \tag{16}$$

$$F_\tau = \mathcal{F}_\tau[1 + c_{R2} R(\dot{\xi})] \tag{17}$$

where, however, $\operatorname{asinh}(\dot{\varepsilon}/C_1)$ is replaced by function $R(\dot{\xi})$ of global strain rate measure $\dot{\xi}$, which satisfies the tensorial invariance restrictions. The following simple definition is used:

$$R(\dot{\xi}) = \operatorname{asinh}(\dot{\xi}/c_{R1}) \approx \ln(2\dot{\xi}/c_{R1}) \quad \text{with } \dot{\xi} = \sqrt{\tfrac{1}{2}\dot{\varepsilon}_{ij}\dot{\varepsilon}_{ij}} \tag{18}$$

where the logarithmic approximation of R is admissible only if $\dot{\xi}^2 \gg c_{R1}$; c_{R1}, c_{R2} are material rate constants, analogous to C_1, which have been calibrated by test data. They can be considered as fixed parameters, which need not be adjusted by the user and are applicable to all concretes; $\dot{\varepsilon}_{ij}$ are strain rate components with subscripts i,j $(=1,2,3)$ referring to Cartesian components, and repetition of subscripts implies summation; and $\dot{\xi}$ is a non-negative invariant of $\dot{\varepsilon}_{ij}$ (note that the square root of the second invariant of the strain rate tensor would be inappropriate because the cracking strain involves volume change).

5.2. Viscoelastic rate effect

The viscoelasticity (or creep) of concrete is properly taken into account at the microplane level. The creep is fully characterized by the compliance function $J(t,t')$, representing the strain at time t caused by a unit uniaxial stress applied at time t', and by the creep Poisson ratio ν, which can be approximately taken as constant ($\nu=0.18$). The constitutive law, based on the principle of superposition, consists of a matrix integral equation over the stress tensor history. For the analysis of impact and penetration, the aging of concrete may be neglected. In that case $J(t,t')\approx J(t-t')=$ function of only the time lag $t-t'$. Computationally it is more effective to approximate the integral-type constitutive law with a Kelvin chain or Maxwell chain. This leads to a system of first-order matrix differential equations in time for the partial strains or stresses of the chain, whose values from the preceding time step need to be stored.

Since long-time creep is not of interest here, the entire Maxwell chain is not needed. Therefore (in similarity to the approach of Ožbolt and Bažant, 1992), the compliance function may be approximated for the duration of loading (e.g., the impact event) by a single spring-dashpot Maxwell rheologic model (see Fig. 1d in Bažant et al., 2000a). For uniaxial stress, this model is characterized by the stress strain relation:

$$\dot{\varepsilon}=\frac{\dot{\sigma}}{E}+\frac{\sigma}{\eta} \tag{19}$$

where $E=$ elastic modulus and $\eta=$ viscosity.

Assuming that, during each time step Δt, the strain rate $\dot{\varepsilon}$ is constant, the solution of Eq. (19) within the time step beginning at time t_i is

$$\sigma(t)=\eta\dot{\varepsilon}+(\sigma_i-\eta\dot{\varepsilon})\,\mathrm{e}^{-E(t-t_i)/\eta} \tag{20}$$

Setting $t=t_i+\Delta t$ and $\dot{\varepsilon}\approx\Delta\varepsilon/\Delta t$, this may be rearranged to the following quasi-elastic incremental stress–strain relation

$$\Delta\sigma=E''\Delta\varepsilon-\Delta\sigma'' \tag{21}$$

with the notations

$$E''=\frac{1-\mathrm{e}^{-\zeta}}{\zeta}E,\quad \Delta\sigma''=\left(1-\mathrm{e}^{-\zeta}\right)\sigma,\quad \zeta=\Delta t/\tau_1 \tag{22}$$

where σ is the value at the beginning of the time step Δt, and $\tau_1=\eta/E=$ relaxation time of the Maxwell model. Eq. (22) define the exponential algorithm for linear viscoelasticity (Bažant, Chairman, 1988). Unlike the central difference algorithm, this algorithm is unconditionally stable no matter how large the ratio ζ is. Note that, in computer calculations, an overflow may occur in Eq. (22) when ζ is very small. To prevent it, the first terms of the Taylor series expansions of E'' and $\Delta\sigma''$ must be used for very small ζ.

5.3. Discussion of quasi-static rate effects

Numerous test data on the apparent unconfined compressive strength under uniaxial compression of various concretes show that, with increasing strain rate, the apparent strength increases sharply (see Fig. 1 in Cotsovos and Pavlović, 2008). These data can be predicted well up to a strain rate of about $1\ \mathrm{s}^{-1}$ by model M7 with quasi-static rate effect, and also by other models that incorporate the activation energy based rate effect. But at higher strain rates, a proper comparison of model predictions with experimental results would require the strain rate distributions across the specimen. However, it is next to impossible to record these distributions in experiments at very high rates of loading. The numerical model predictions of what is left of the specimen body can also be compared to the remains of the specimens tested. For example, the so-called lattice discrete particle models (e.g. Cusatis et al., 2003, 2011a,b) can predict the mesoscale fragmentation behavior of the specimens during high strain rate tests, though not yet the comminution on a finer scale. Continuum models such as model M7 can be used to simulate approximately the effects of both the mesoscale fragmentation and finer scale comminution, for example, by deleting the failed elements and lumping the deleted element masses to rigid particles at the nodes. The geometric shape that consists of the surviving elements at the end of the simulation can be compared to the surviving specimen parts from the experiments.

The confined compression behavior at high strain rates of concrete is of interest for perforation of concrete slabs by projectiles as well as explosions. Forquin et al. (2008) reported Hopkinson pressure bar tests of concrete “MB50” cast in a steel tube. In these tests, shock waves are generated to create the desired strain rate in the concrete core of the specimens. To calibrate model M7, only the Young modulus has been adjusted to $E=70$ GPa, while the other model parameters have been considered with their reference values reported in Caner and Bažant (2013b). The values of quasistatic strain-rate

parameters were determined as $C_{R1} = 4 \times 10^{-6}$ and $C_{R2} = 0.022$. Fig. 4a depicts the hoop strain test data measured by strain gauge G3 and their predictions by model M7. The predictions by model M7 are completely satisfactory.

Next, using model M7 calibrated for the "MB50" concrete used in these tests, the axial stress–strain response of that concrete to high strain rates is extracted, as shown in Fig. 4b. The responses for the strain rates 141 s^{-1} and 221 s^{-1} are visually indistinguishable, meaning the continuous curve in that figure is probably the maximum response that can be obtained for such concretes cast in steel tubes using the activation energy based rate effect theory. The dashed curve in this figure corresponds to quasi-static laboratory strain rates. These results indicate that, when the inertial effects are minimized, a relatively small strain rate effect exists in the response of concrete under confinement even when the strain rates are significantly larger than the quasi-static rates.

6. Comminution rate effect in model M7 and simulations of missile penetration

The sharp increase of the strength amplification factor for strain rates above 10 s^{-1} (e.g. see Fig. 1 in Cotsovos and Pavlović, 2008 or Fig. 1 in Bažant and Caner, this issue) documents that good prediction of the exit velocities of projectiles is hardly possible using only quasi-static strain rate effects. This is documented by Fig. 3 showing the calculation results for microplane model M7 calibrated for the WES-5000 concrete. To resolve the strain rates and keep the discretization error low, small enough tetrahedral elements (of size 7.5 mm) have been employed in the finite element analyses. Both the compression and tension performance of these elements employing the M7 constitutive model have been verified.

A series of finite element calculations of projectile perforation have been performed using model M7 with only the quasi-static strain rate effects. The results are shown as the dashed curve in Fig. 5. The calculated exit velocities far exceed the experimental values. Thus, the quasi-static rate effects are clearly insufficient to explain the observed exit velocities of these projectiles.

It should be mentioned that these velocities could roughly be obtained by calculations with an enhanced friction coefficient. However, assuming a higher friction coefficient for high slip rates is questionable since other experimental

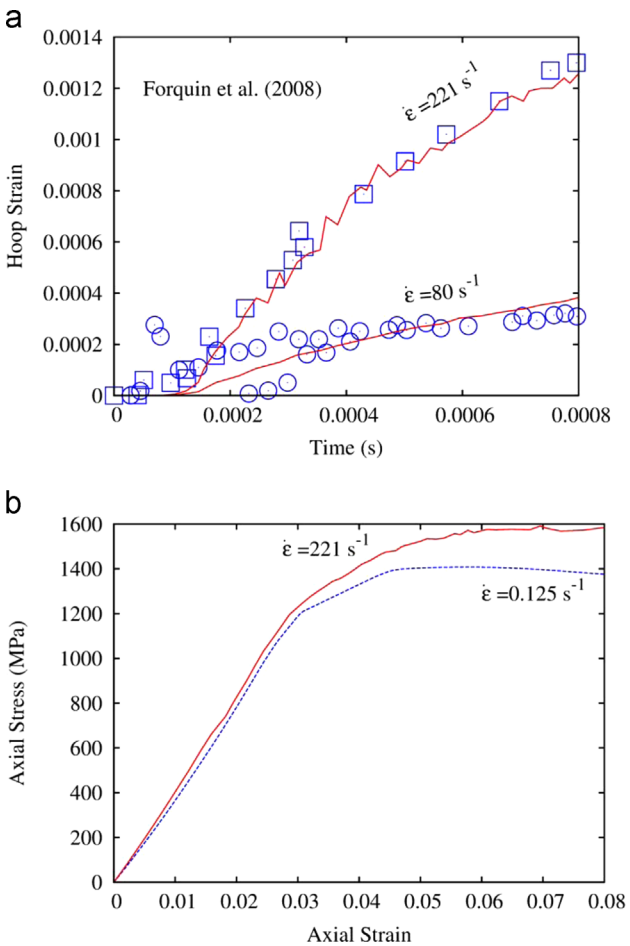

Fig. 4. (a) Comparison of hoop strain test data at strain rates of 80 s^{-1} and 221 s^{-1} of MB50 concrete cast in steel tubes (symbols) and predictions by the model M7 (lines); (b) axial stress–strain behavior of MB50 concrete at quasistatic strain rates (dashed line) and at a strain rate of 221 s^{-1} (continuous line).

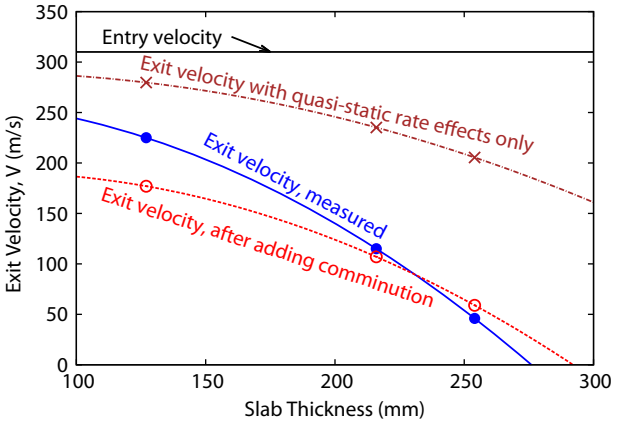

Fig. 5. Comparison of measured exit velocities and predictions by model M7 using only quasi-static strain rate effect and both quasi-static strain rate effect and effect of comminution of concrete.

evidence shows the friction coefficient to decrease with an increasing slip rate. Also, a blunter nose profile different from the one used in the tests could help to reduce the penetration velocity.

It was also examined whether the effect of the frictional boundary, which can greatly increase with the confining pressure, could suffice to explain the drop of exit velocities for thicker walls. However, the calculated confining pressure was not high enough. Actually, in absence of large enough pressure on the missile sides, the dynamic sliding leads to a reduction of friction. Thus, although the rate effect is here applied also at the microplane frictional boundary, it is ineffective in reducing the missile speed and cannot explain the observed exit velocities.

In Frank et al. (2012), the entry and exit crater geometries, as well as the exit velocities of the projectiles, were matched by imposing on microplane model M4 a major empirical expansion of the static microplane stress–strain boundaries (or strain-dependent yield limits) determined so as to fit the penetration data. The expansion was both vertical and horizontal. Although the vertical expansion of these microplane yield limits might be explained by the comminution effect (coupled with the quasi-static rate effects), a horizontal expansion of these boundaries can hardly be justified theoretically. In fact, a horizontal expansion of the boundaries implies an increase of ductility, but the existing experimental evidence indicates that, as the strain rate increases, concrete becomes more brittle. Still more importantly, the fracture energy is known not to change much with the strain rate (Jansen et al., 1995; Yon et al., 1992).

Another significant parameter of the perforation of concrete slabs is the shape of the projectile tip. Intuitively, a blunt projectile would be less effective than a sharp one in perforating slabs. The projectile tip has been specified in Frank et al. (2012) as an ogive nose with a caliber radius head of 3.0 and a length to diameter ratio of 7. The diameter of the projectile was 50.8 mm. For the definition of the caliber radius head, the formula given in Simms and Berger (2010) can be used. More details of the dimensions of the projectile are given in Cargile (1999).

The impossibility of predicting the correct exit velocities of the projectiles with the same quasi-static rate-dependent microplane constitutive law and the same element sizes revealed that there must be a different type of rate effect that dissipates far more energy than the quasi-static rate effect. In the preceding companion paper (Bažant and Caner, this issue), it is postulated that this rate effect arises from the comminution of material into very fine particles at extremely high strain rates. This comminution rate effect has been implemented as a nonlinear viscous element (or dashpot) which is coupled in parallel with the microplane model and generates the shear viscosity

$$\eta_D = \frac{\Gamma}{\tau_0}\left(\frac{C_0^{2/3} G\rho}{C_g}\frac{B_a}{1+B_a^2}\right)^{1/2} \tag{23}$$

leading to the comminution induced shear stress tensor given by

$$\tau_{ij} = \eta_D \dot{e}_{ij} \tag{24}$$

where $\dot{e}_{ij} = \dot{\varepsilon}_{ij} - \delta_{ij}\dot{\varepsilon}_{kk}$ and $\eta_D =$ shear viscosity; B_a is the dimensionless number characterizing the ratio of kinetic energy of shear strain rate to the maximum possible strain energy, defined in Part I along with C_0 and G_g.

Fig. 5 shows, by dashed curves with circles, the exit velocities of projectiles predicted by three different versions of model M7:

(1) basic M7 for quasi-static multiaxial behavior of concrete;
(2) M7 enhanced by the quasi-static strain rate effects (which include the crack opening rate and viscoelasticity); and
(3) M7 with the comminution rate effect and the quasi-static rate effects.

The exit velocity predictions which include the effect of comminution are clearly superior.

Model M7 including all of these rate effects has been coded into VUMAT subroutine of ABAQUS. The finite element analysis of the perforation of concrete walls was performed in the sense of crack band model. In these perforation simulations, the slabs are discretized uniformly using 4-node constant strain tetrahedral elements of size approximately 7.5 mm. The effect of switching to higher-order elements has been found negligible, in both crater formation and exit velocities, except for an increase in the computational cost of each simulation.

The boundary effects, such as wave reflection at the boundary of the mesh, have been removed in some of the simulations by attaching a single layer of infinite (or wave transmitting) finite elements at all exterior boundaries. But the removal of these boundary effects has resulted in negligible changes in both crater formation and exit velocities. By contrast, in explosion simulations, the boundary effects are known to play a crucial role in the degree of damage inflicted upon a concrete slab.

The crater geometries in three dimensions and a half of the projectile are shown in Fig. 6a–c for slab the thicknesses of 127 mm, 216 mm and 254 mm respectively. The thick black line represents the measured profile of the craters (see Fig. 3 in Frank et al., 2012). In the simulations, the elements whose maximum principal strain reached 0.005 or more have been eroded so that the computer simulation could proceed (otherwise the maximum time increments allowed by numerical stability would become too short and the computer simulation would abort). This threshold of element erosion corresponds

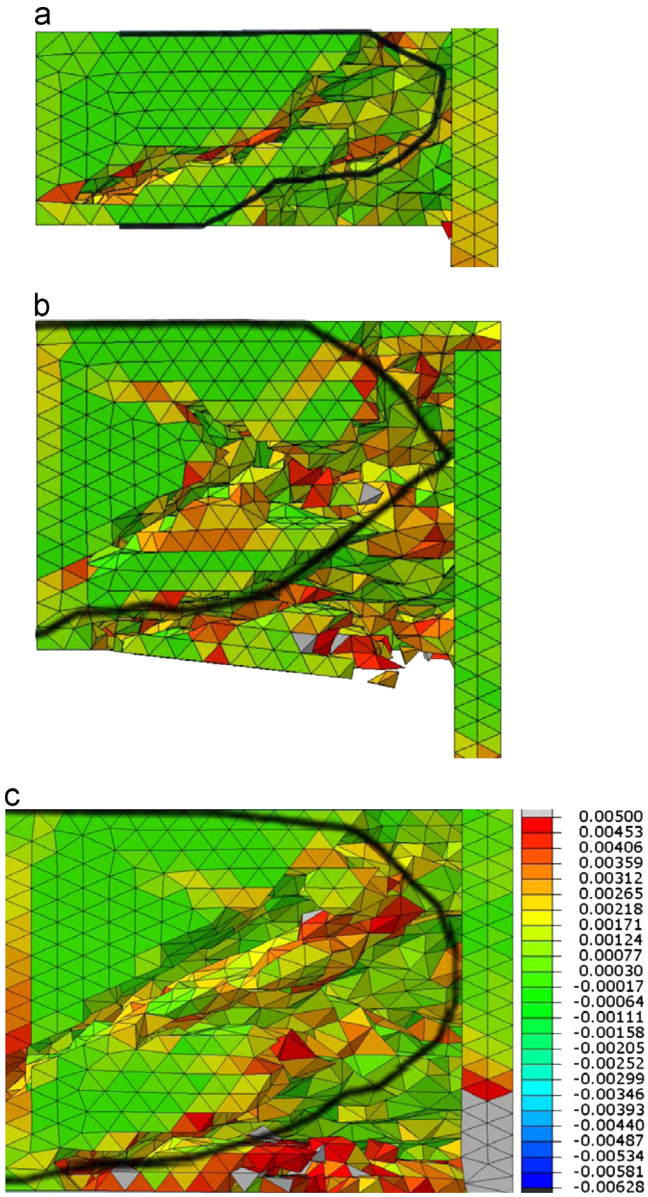

Fig. 6. Comparison of measured crater shapes (thick black curve) and predictions by model M7 using both quasi-static strain rate effect and effect of comminution of concrete in slabs of thickness (a) 127 mm, (b) 216 mm, (c) 254 mm and the legend for max. principal strains.

to material failure in the direction of the maximum principal strain under quasi-static loading conditions. Failure is assumed even though some of these eroded elements might still be carrying some compressive stress perpendicular to the maximum tensile stress direction.

7. Uncertainties and errors due to possible effects of moisture content, age, curing, etc.

The overestimation of the exit velocity of the thin slabs might not be an error of the present theory. It might be caused by various extraneous factors. For example, since the thinner slabs dry faster, the thin slab must have had a lower specific moisture content than the thicker one if the curing type and durations were about the same. Hopkinson bar tests reported in Cadoni et al. (2001) showed that a lower moisture content of concrete can lead to a significant decrease of strength under high-rate loading. This increase might explain why the measured exit velocity for the thin (and thus drier slab) is lower than the present prediction shown in Fig. 5. However, the data are so limited that no meaningful calculations are possible at this time. Especially, it is not clear whether the slab were tested right after moist curing, or whether they were exposed to drying before the test, and whether the period of drying exposure was the same for each slab. The environmental humidity and the permeability of concrete are also not known.

There are further factors that could have skewed the result. From Cargile (1999) it is not clear whether the specimens had the same age at the time of the tests and whether they experienced the same environmental and curing history. For example, if the thinner slab was appreciably older than the thicker ones, the chemical process of hydration could have caused the strength and fracture energy of the thin slabs to be significantly higher than it was in the thicker slabs. Furthermore, according to Cargile (1999), the slabs were clearly not cast from the same batch of concrete, and thus random differences between different batches of the same concrete might have caused strength differences as high as 8%.

So it is at present impossible to conclude whether the overestimation of the exit velocity of the thin plate, seen in Fig. 5, is an error of the present theory, or an error of the data themselves. Further experiments are needed.

8. Conclusions

1. If only the quasi-static rate effects due to crack opening rate and to viscoelasticity are taken into account, the observed exit velocities in the perforation of concrete slabs by projectiles cannot be matched by computer simulations.
2. Missile penetration can produce strain rates on the order of $10^5\ s^{-1}$. Such strain rates must be causing comminution of concrete resulting in dissipation of enormous energy.
3. Comminution of concrete at such extremely high strain rates can explain the additional dissipation needed to match the exit velocities of perforating projectiles.
4. The simulation results agree with the theoretical prediction that the comminution is equivalent to additional shear stresses of concrete proportional to the 2/3-power of deviatoric strain rate, which is in turn equivalent to a deviatoric (shear) viscosity proportional to the $-1/3$-power of the deviatoric strain rate.
5. Including in the calculations a comminution due to rate of volume expansion has almost no effect on the exit velocities of the projectiles. Hence, the comminution must be explained in terms of the shear strain rate.
6. Including a strain-rate dependent friction between the projectile and the surrounding concrete cannot help to explain the additional dissipation needed to match the exit velocities.
7. The underestimation of the exit velocity of the thinnest slab might be explicable by taking into account the Hopkinson bar tests indicating that a drier concrete has a lower strength, and thus less resistance to missile penetration. However, the data are too scant for meaningful calculations. The underestimation could easily be explained by possible defects in the design and control of the experiments and by missing data on water content, age, curing, etc.
8. The microplane model M7 coupled with both the comminution rate effect and the quasi-static strain rate effects can correctly predict the geometries of the both the entry and exit craters and gives overall a satisfactory match of the observed exit velocities of the projectiles.

Acknowledgments

The first author gratefully acknowledges the financial support from ENRESA under contract no. 79000136 with the Technical University of Catalonia. Support during the initial phase of research under Grant W911NF-09-1-0043/P00003 from the U.S. Army Research Office, Durham, to Northwestern University is also gratefully acknowledged. The Agency for Defense Development (ADD), Korea, is thanked for supporting the subsequent work on the dynamic comminution theory and its use in microplane model simulations of projectile perforations under a Daejeon University Grant to Northwestern University.

References

Adley, M.D., Frank, A.O., Danielson, K.T., 2012. The high-rate brittle microplane concrete model: Part I: bounding curves and quasi-static fit to material property data. Comput. Concr. 9, 293–310.

Batdorf, S., Budianski, B., 1949. A mathematical theory of plasticity based on the concept of slip. Technical Note 1871. National Advisory Committee for Aeronautics. Washington, D.C.
Bažant, Z., 1984. Microplane model for strain-controlled inelastic behavior. In: Desai, C.S., Gallagher, R.H. (Eds.), Mechanics of Engineering Materials. John Wiley, London, pp. 45–59. (Chapter 3).
Bažant, Z.P., Caner, F.C. Impact comminution of solids due to local kinetic energy of high shear strain rate: I. Continuum theory and turbulence analogy. J. Mech. Phys. Solids, this issue.
Bažant, Z.P., Caner, F.C., Adley, M.D., Akers, S.A., 2000a. Fracturing rate effect and creep in microplane model for dynamics. ASCE J. Eng. Mech. 126, 962–970.
Bažant, Z.P., Caner, F.C., Carol, I., Adley, M.D., Akers, S.A., 2000b. Microplane model M4 for concrete: I. Formulation with work-conjugate deviatoric stress. ASCE J. Eng. Mech. 126, 944–953.
Bažant, Z.P., Li, Y.N., 1997. Cohesive crack with rate-dependent opening and viscoelasticity: I. Mathematical model and scaling. Int. J. Fract. 86, 247–265.
Bažant, Z.P., Oh, B.H., 1985. Microplane model for progressive fracture of concrete and rock. ASCE J. Eng. Mech. 111, 559–582.
Bažant, Z.P., Prat, P.C., 1988. Microplane model for brittle plastic material: I. Theory. ASCE J. Eng. Mech. 114, 1672–1688.
Butler, G.C., McDowell, D.L., 1998. Polycrystal constraint and grain subdivision. Int. J. Plasticity 14, 703–717.
Cadoni, E., Labibes, K., Albertini, C., Berra, M., Giangrasso, M., 2001. Strain-rate effect on the tensile behaviour of concrete at different relative humidity levels. Mater. Struct. (RILEM, Paris) 34 (January–February), 21–26.
Caner, F.C., Bažant, Z.P., 2000. Microplane model M4 for concrete: II. Algorithm and calibration. ASCE J. Eng. Mech. 126, 954–961.
Caner, F.C., Bažant, Z.P., 2013a. Microplane model M7 for plain concrete: I. Formulation. ASCE J. Eng. Mech. http://dx.doi.org/10.1061/(ASCE)EM.1943-7889.0000570.
Caner, F.C., Bažant, Z.P., 2013b. Microplane model M7 for plain concrete: II. Calibration and verification. ASCE J. Eng. Mech. http://dx.doi.org/10.1061/(ASCE)EM.1943-7889.0000571.
Caner, F.C., Bažant, Z.P., Wendner, R., 2013. Microplane model M7f for fiber reinforced concrete. Eng. Fract. Mech. 105, 41–57.
Cargile, J.D., 1999. Development of a constitutive model for numerical simulations of projectile penetration into brittle geomaterials. Technical Report SL-99-11. U.S. Army Engineer Research and Development Center. Vicksburg, MS.
Cotsovos, D.M., Pavlović, M.N., 2008. Numerical investigation of concrete subjected to compressive impact loading. Part I: a fundamental explanation for the apparent strength gain at high loading rates. Comput. Struct. 86, 145–163.
Cusatis, G., Bažant, Z.P., Cedolin, L., 2003. Confinement-shear lattice model for concrete damage in tension and compression: I. Theory. ASCE J. Eng. Mech. 129, 1439–1448.
Cusatis, G., Mencarelli, A., Pelessone, D., Baylot, J.T., 2011a. Lattice discrete particle model (LDPM) for failure behavior of concrete. II: calibration and validation. Cem. Concr. Compos. 33, 891–905.
Cusatis, G., Pelessone, D., Mencarelli, A., 2011b. Lattice discrete particle model (LDPM) for failure behavior of concrete. I: theory. Cem. Concr. Compos. 33, 881–890.
Doyoyo, M., 2002. A theory of the densification-induced fragmentation in glasses and ceramics under dynamic compression. Int. J. Solids Struct. 39, 1833–1843.
Forquin, P., Gary, G., Gatuingt, F., 2008. A testing technique for concrete under confinement at high rates of strain. Int. J. Impact Eng. 35, 425–446.
Frank, A.O., Adley, M.D., Danielson, K.T., McDevitt, H.S., 2012. The high-rate brittle microplane concrete model: part II: application to projectile perforation of concrete. Comput. Concr. 9, 311–325.
Jansen, D.C., Shah, S.P., Rossow, E.C., 1995. Stress–strain results of concrete from circumferential strain feedback control testing. ACI Mater. J. 92, 419–428.
Krausz, A., Krausz, K., 1988. Fracture Kinetics of Crack Growth. Kluwer, Dordrecht.
Li, Y.N., Bažant, Z., 1997. Cohesive crack with rate-dependent opening and viscoelasticity: II. Numerical algorithm, behavior and size effect. Int. J. Fracture 86, 267–288.
Ožbolt, J., Bažant, Z., 1992. Microplane model for cyclic triaxial behavior of concrete. ASCE J. Eng. Mech. 118, 1365–1386.
Rice, J., 1971. Inelastic constitutive relations for solids: an internal variable theory and its application to metal plasticity. J. Mech. Phys. Solids 19, 433–455.
RILEM Committee TC 69 (Z.P. Bažant, Chairman), 1988. State of the art in mathematical modeling of creep and shrinkage of concrete. In: Bažant, Z.P. (Ed.), Mathematical Modeling of Creep and Shrinkage of Concrete. John Wiley, Chichester, New York, pp. 57–215.
Simms, J.E., Berger, R.P., 2010. Demonstration of UXO-PenDepth for the estimation of projectile penetration depth. Technical Report MR-0806. US Department of Defense. ESTCP Project.
Taylor, G., 1938. Plastic strain in metals. J. Inst. Metals 62, 307–324.
Yon, J.H., Hawkins, N.M., Kobayashi, A.S., 1992. Strain-rate sensitivity of concrete mechanical properties. ACI Mater. J. 89, 146–153.